Fully nonlinear mode competitions in magnetised Taylor-Couette flow

R. Ayats[1], K. Deguchi[2], F. Mellibovsky[1] and A. Meseguer[1] †

[1]Departament de Física, Universitat Politècnica de Catalunya, 08034, Barcelona, Spain
[2]School of Mathematics, Monash University, VIC 3800, Australia

We study the nonlinear mode competition of various spiral instabilities in magnetised Taylor-Couette flow. The resulting finite-amplitude mixed-mode solution branches are tracked using the annular-parallelogram periodic domain approach developed by Deguchi & Altmeyer (2013). Mode competition phenomena are studied in both the anti-cyclonic and cyclonic Rayleigh-stable regimes. In the anti-cyclonic sub-rotation regime, with the inner cylinder rotating faster than the outer, Hollerbach, Teeluck & Rüdiger (2010) found competing axisymmetric and non-axisymmetric magneto-rotational linearly unstable modes within the parameter range where experimental investigation is feasible. Here we confirm the existence of mode competition and compute the nonlinear mixed-mode solutions that result from it. In the cyclonic super-rotating regime, with the inner cylinder rotating slower than the outer, Deguchi (2017) recently found a non-axisymmetric purely hydrodynamic linear instability that coexists with the non-axisymmetric magneto-rotational instability discovered a little earlier by Rüdiger, Schultz, Gellert & Stefani (2016). We show that nonlinear interactions of these instabilities give rise to rich pattern-formation phenomena leading to drastic angular momentum transport enhancement/reduction.

1. Introduction

The objective of this study is the nonlinear interactions between various instability modes occurring in magnetised Taylor-Couette flow, i.e. the fluid flow between independently rotating concentric cylinders. The purely hydrodynamic Taylor-Couette flow, in the absence of magnetic field, has long served as a theoretical, numerical and experimental test bench for the study of centrifugal and shear instability mechanisms. Keeping the outer cylinder stationary, Taylor (1923) observed that the flow is destabilised by purely hydrodynamic axisymmetric perturbations at a certain critical speed of the inner cylinder. The balance between rotational and shear effects can be modified by further introducing a rotation of the outer cylinder. The independent variation of the inner and outer cylinder speeds results in a rich diversity of secondary nonlinear flow patterns, as reported by Andereck *et al.* (1986). The stability and nonlinear states of Taylor-Couette flow are commonly studied in the R_i–R_o parameter space schematically depicted in figure 1, where R_i and R_o are the Reynolds numbers associated with the inner and outer cylinder speeds, respectively. In accordance with the symmetries of the problem, the R_i-R_o parameter plane is invariant to π-rotation about the origin, such that only the upper half plane needs to be explored. The right/left half of the semi-plane

---

† Email address for correspondence: roger.ayats@upc.edu, kengo.deguchi@monash.edu, fernando.mellibovsky@upc.edu, alvaro.meseguer@upc.edu
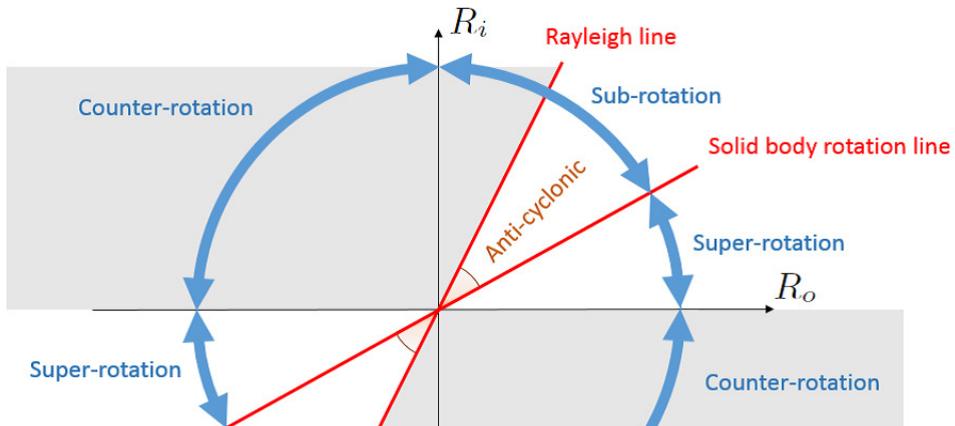
FIGURE 1. R_i–R_o parameter space representation of Taylor-Couette flow. The plane is divided into the counter-rotation and the co-rotation regimes. This latter is further subdivided into sub-rotation and super-rotation by the solid-body rotation line defined by equal angular speed of both cylinders. The shaded regions denote inviscid instability of circular Couette flow following the Rayleigh criterion. The portion of the subrotation regime comprised between the Rayleigh and solid-body rotation lines goes by the name of anti-cyclonic regime (also called *Quasi-Keplerian*), while the rest of the plane is called cyclonic.

corresponds to cylinders rotating in the same/opposite direction (i.e. co-rotation/counter-rotation). The first quadrant (co-rotation regime) is divided into sub-rotation and super-rotation by the solid-body rotation line (equal angular speed of the cylinders), depending on whether the outer cylinder rotates slower or faster than the inner. For any given speed of the outer cylinder, Rayleigh's inviscid stability criterion establishes that circular Couette flow remains centrifugally stable to infinitesimal axisymmetric perturbations as long as the inner cylinder is steady or in co-rotation up to a certain speed, delimited by the so-called Rayleigh line (the wedge-shaped white region in figure 1 comprised between the Rayleigh line and the horizontal $R_i = 0$ line). Taking viscous effects and non-aximsymmetric perturbations into account affects the stability boundaries, but it is widely accepted that the Rayleigh line acts as a fairly approximate threshold below which circular Couette flow remains the only stable state, given that no experimental or numerical evidence of nonlinear flow states has been found to date (see Ji *et al.* 2006; Edlund & Ji 2014; Lopez & Avila 2017). Note however that no first-principle theory has been advanced so far to support the nonlinear hydrodynamic stability in the quasi-Keplerian flow regime (see Balbus 2017, for a summary on the matter).

The Rayleigh-stable region is further subdivided into the *anti-cyclonic* and *super-rotation cyclonic* regimes by the solid body rotation line, corresponding to both cylinders rotating at the same angular speed. Immediately to the right of the Rayleigh line and all the way down to solid rotation, (co-rotation and sub-rotation) is said to be *anti-cyclonic* and laminar Couette flow is allegedly linearly stable. This region is of utmost astrophysical interest, since Keplerian rotational flow, a vastly used model for accretion disks, is precisely anti-cyclonic. The rate at which angular momentum is radially transported in astrophysical accretion disks observation requires the flow to be turbulent. This has motivated a wealth of studies (see the review paper Rüdiger *et al.* (2018a)) exploring magneto-rotational instabilities (henceforth referred to as MRI) as a possible alternative source for turbulence in a flow that appears otherwise to always revert back to laminar in the absence of magnetic fields. The pioneering works by Velikhov (1959) and

Chandrasekhar (1960) showed that a uniform external magnetic field in the axial direction indeed destabilises the anti-cyclonic regime, while the importance of the instability in the astrophysical context was noted for the first time by Balbus & Hawley (1991). This type of MRI is nowadays called the *standard* type of MRI, SMRI for short.

A different approach was nevertheless taken in the first experimental observation of the MRI (Stefani *et al.* 2006). The SMRI is actually very difficult to reproduce in liquid metal experiments where the magnetic Prandtl number P_m is very small, as magnetic induction is essential in this case. As shown by Goodman & Ji (2002), the critical Reynolds number of the SMRI is inversely proportional to the magnetic Prandtl number P_m for small P_m, meaning that the cylinders must rotate at an extremely fast rate to trigger the SMRI in the experimental apparatus. The crux in reproducing a MRI at relatively small Reynolds numbers was the numerical finding by Hollerbach & Rüdiger (2005) that, when both azimuthal and axial external magnetic fields are applied simultaneously, the critical Reynolds number saturates at a finite value even in the inductionless limit of $P_m \to 0$. Soon after the discovery of this *helical* MRI (henceforth referred to as HMRI), growth of axisymmetric perturbations was confirmed in the series of PROMISE experiments (Stefani *et al.* 2006, 2007; Rüdiger *et al.* 2006). Later on, Hollerbach *et al.* (2010) found that non-axisymmetric modes arise instead when purely azimuthal magnetic fields are considered in the sub-rotation regime just below the Rayleigh line. They further showed that these so-called azimuthal magneto-rotational instability (AMRI) modes persist when a small axial magnetic field is added to the predominantly azimuthal field, thus implying that they could potentially interact with the axisymmetric HMRI mode. In fact, when the strength of the azimuthal and axial external magnetic fields are suitably adjusted, the critical Reynolds numbers for the axisymmetric and non-axisymmetric modes become comparable. The competition of these modes may yield rich nonlinear flow patterns at this particular HMRI regime. This nonlinear mode interaction is the first subject we will tackle in this study.

In the early years of the pattern-formation theoretical studies in purely hydrodynamic Taylor-Couette flow, weakly nonlinear analysis was employed to investigate mode interactions among multiple linear instability modes near criticality (e.g. Davey *et al.* 1968; Iooss 1986; Golubitsky *et al.* 1988; Chossat & Iooss 1994). The simplest mode interaction occurs between two identical but mutually-symmetric, with respect to an axial reflection, spiral modes. In this case, the fully nonlinear mixed-mode solution can be computed in numerical simulations using a periodic axial-azimuthal orthogonal domain (Tagg *et al.* 1989). However, when the interacting spirals are not mutually symmetric and have a different absolute pitch, as are indeed the two mode interactions studied here, the numerical computation of the fully nonlinear mixed mode is no longer straightforward. The periodic computational domain must fit an integer number of both constituent modes in order to faithfully reproduce the mixed mode, which may lead to unaffordably large domains. This may be feasible in some occasions (Pinter *et al.* 2006; Avila *et al.* 2006; Altmeyer & Hoffmann 2010), but it is at the very least inefficient from a computational point of view, if not altogether prohibitive. A convenient methodology for the computation of general mixed-mode states was provided by Deguchi & Altmeyer (2013), who realised that the infinite annulus might be subdivided into a regular tiling of a suitable parallelogram-shaped periodic box that can be chosen optimally small for any flow pattern arising from nonlinear interaction of two modes, as we are considering here. Extension of the nonlinear code to magnetised problems might prove highly valuable to the study of MRI, as nonlinear simulations in cylindrical/annular domains have only recently been undertaken (Guseva *et al.* 2015, 2017).

In the second half of this paper we shall also study the nonlinear mode competitions

occurring in the other Rayleigh stable regime, i.e. the super-rotation regime seen in figure 1. Recently, magnetohydrodynamic instabilities in this regime have attracted much attention as they are thought to be relevant for turbulence generation in a part of Sun's tachocline. In this second subject we shall investigate the nonlinear competition of two recently discovered linear instability modes.

For the purely hydrodynamic problem, nonlaminar flow patterns in the inviscidly stable super-rotation regime were first reported several decades ago in Taylor-Couette experiments by Wendt (1933) and Coles (1965), but at the time it was not clear whether the instability was legitimate or an end-wall effect induced by the cylinder lids. Advance in computational power eventually allowed to numerically confirm the existence of subcritical spiral turbulence and intermittency found experimentally (Van Atta 1966; Prigent *et al.* 2002; Hegseth *et al.* 1989; Burin & Czarnocki 2012) in the counter-rotation regime in the absence of end-wall effects (Meseguer *et al.* 2009; Dong 2009). Nonlinear coherent states have indeed been followed into the super-rotation regime, crossing the $R_i = 0$ boundary, as illustrated by the computation of the first rotating wave in cyclonic super-rotation (Deguchi, Meseguer & Mellibovsky 2014) and by direct numerical simulation (Ostilla-Monico, Verzicco & Lohse 2016). All non-trivial flow patterns hitherto observed in super-rotation are finite amplitude and highly nonlinear, such that they by no means belie the widely assumed linear stability of super-rotating hydrodynamic Taylor-Couette flow, in view of countless numerical studies of the neutral curve (see the review article by Grossmann *et al.* (2016)). The recent unexpected discovery by Deguchi (2017) of a linear instability in the super-rotation regime came therefore as a big surprise. Considering non-axisymmetric perturbations and a relatively long axial wavelength were key ingredients to the finding. This instability mode of a purely hydrodynamic nature, hereafter called the D17 mode, is the first of the two modes we shall consider in our second mode competition study.

The other mode at play inherently originates from the MRI mechanism and is called the super-AMRI (Rüdiger, Schultz, Gellert & Stefani 2016, 2018*b*), where the prefix *super* refers to the super-rotation regime. This mode belongs, along with the usual forms of HMRI and AMRI for sub-rotation, to the class of inductionless MRI. It has long been known that MRI is not easily triggered in the super-rotation regime for the axisymmetric case. For ideal fluids, Velikhov's condition states that the axial magnetic field cannot destabilise this regime (Velikhov 1959), while according to Michael's condition (Michael 1954), an azimuthal field can only be destabilising provided its modulus increases outwards at a sufficiently fast rate. Moreover, when the azimuthal magnetic field is current-free, it can be formally shown that axisymmetric MRI are impossible in spite of the diffusive effect (Herron & Soliman 2006). A breakthrough regarding instability in the cyclonic super-rotation regime is due to Stefani & Kirillov (2015), who pointed out that for sufficiently narrow gaps the non-axisymmetric instability could be continued into the super-rotation regime using the so-called local approximation and the inductionless limit ($P_m \to 0$). However, the existence of the super-AMRI was not conclusive at this stage given that a local approximation does not always necessarily provide accurate insight into the global problem. Soon after, conclusive numerical evidence of the super-AMRI was reported by Rüdiger *et al.* (2016, 2018*b*), who concluded that the destabilisation seems to occur for fairly arbitrary magnetic field profiles as long as the flow is double-diffusive, i.e. $P_m \neq 1$.

The paper is organised as follows. Section §2 formulates the problem based on the inductionless limit of the magneto-hydrodynamic equations. The section addresses in detail the numerical discretization of the equations in annular-parallelogram periodic domains and, in particular, describes the Newton solver for the computation of nonlinear mixed-mode travelling waves using the transformed coordinate system and a suitable

co-moving reference frame. Section §3 is devoted to the anti-cyclonic regime. The helical magnetic field is imposed to find the nonlinear mixed-mode solutions that arise from the mode competition advanced by Hollerbach *et al.* (2010). The first part of section §4 deals with the interaction between the classical non-axisymmetric and the D17 modes in purely hydrodynamic counter-rotating Taylor-Couette flow. In the second half of the section we shall see how an imposed azimuthal magnetic field alters the nature of this interaction. Finally, in section §5, we briefly summarise the results and present concluding remarks.

2. Formulation of the problem

Consider an electrically conducting fluid of density ρ^*, kinematic viscosity ν^*, and magnetic diffusivity η^*, confined between two concentric cylinders of inner and outer radii r_i^* and r_o^*, independently rotating at angular speeds Ω_i^* and Ω_o^*, respectively. In addition, the fluid is subject to the action of a magnetic field of typical strength B_0^*. Throughout the paper we use the length $d^* = r_o^* - r_i^*$, time d^{*2}/ν^*, velocity ν^*/d^*, and magnetic field $\nu^*\sqrt{\rho^*\mu^*}/d^*$ scales for non-dimensionalisation, where μ^* is the magnetic permeability. As a consequence of using the viscous time scale, the Reynolds numbers are absorbed into the expression for the base state flow fields and disappear form the non-dimensional equations for the perturbation. The key parameters of the flow are the radius ratio η, the inner R_i and outer R_o Reynolds numbers, along with the magnetic Prandtl number P_m, and the Hartmann number H:

$$\eta = \frac{r_i^*}{r_o^*}, \quad R_i = \frac{\Omega_i^* r_i^* d^*}{\nu^*}, \quad R_o = \frac{\Omega_o^* r_o^* d^*}{\nu^*}, \qquad P_m = \frac{\nu^*}{\eta^*}, \quad H = \frac{B_0^* d^*}{\sqrt{\rho^*\mu^*\eta^*\nu^*}}. \quad (2.1)$$

The non-dimensional external magnetic field is proportional to $P_m^{-1/2}H$. The reason for using H is that we will consider the so-called inductionless limit $P_m \to 0$ where H is typically fixed as a constant.

Non-dimensionalisation of the velocity $\mathbf{v} = u\mathbf{e}_r + v\mathbf{e}_\theta + w\mathbf{e}_z$ and magnetic $\mathbf{B} = A\mathbf{e}_r + B\mathbf{e}_\theta + C\mathbf{e}_z$ fields, expressed here in cylindrical coordinates (r, θ, z), yields the incompressible viscous-resistive MHD equations

$$\partial_t \mathbf{v} + (\mathbf{v} \cdot \nabla)\mathbf{v} - (\mathbf{B} \cdot \nabla)\mathbf{B} = -\nabla p + \nabla^2 \mathbf{v}, \qquad (2.2a)$$

$$\partial_t \mathbf{B} + (\mathbf{v} \cdot \nabla)\mathbf{B} - (\mathbf{B} \cdot \nabla)\mathbf{v} = P_m^{-1}\nabla^2 \mathbf{B}, \qquad (2.2b)$$

$$\nabla \cdot \mathbf{v} = \nabla \cdot \mathbf{B} = 0, \qquad (2.2c)$$

where p is the total pressure and t is time. Equation (2.2a) expresses momentum conservation, while equation (2.2b) is the induction equation. Equations (2.2c) correspond to continuity and Gauss' law. Along the cylinder walls at radii

$$r_i = \frac{\eta}{1 - \eta}, \qquad r_o = \frac{1}{1 - \eta}, \qquad (2.3)$$

we assume no-slip and perfectly insulating boundary conditions. In our formulation, the velocity and magnetic fields are decomposed into the base and the perturbation flows following

$$\mathbf{v} = v_b(r)\mathbf{e}_\theta + Gw_p(r)\mathbf{e}_z + \widetilde{\mathbf{v}}(r, \theta, z, t), \qquad (2.4a)$$

$$\mathbf{B} = P_m^{-1/2}H\{B_b(r)\mathbf{e}_\theta + C_b(r)\mathbf{e}_z\} + \widetilde{\mathbf{B}}(r, \theta, z, t), \qquad (2.4b)$$

where the tilde denotes perturbation quantities. The pressure perturbation is therefore written as $\widetilde{p}$. Here $v_b(r) = R_s r + R_p r^{-1}$ is the laminar *Couette flow* solution, with

coefficients.

$$R_s = \frac{R_o - \eta R_i}{1 + \eta}, \qquad R_p = \frac{\eta^{-1} R_i - R_o}{1 + \eta} r_i^2, \qquad (2.5)$$

where the subscripts denote the solid-body rotation (s) and the potential (p) components of the flow. External magnetic mechanisms induce the base magnetic fields $B_b(r)$ and $C_b(r)$, which will be duly introduced in (3.1) and (4.1) for the two types of predominantly azimuthal fields that will be considered throughout the paper.

We will assume further that there is no axial net mass flux. This is accomplished by imposing an external instantaneously adjustable axial pressure gradient that induces the well-known base *annular Poiseuille flow* profile

$$w_p(r) = (r^2 - r_i^2) \ln r_o + (r_o^2 - r^2) \ln r_i - (r_o^2 - r_i^2) \ln r. \qquad (2.6)$$

The product Gw_p in (2.4a) represents the axial flow induced by the external pressure gradient, whose strength is measured by the coefficient G. That coefficient is a time-dependent additional unknown in the constant mass flux problem. For travelling wave states G is merely a constant. Moreover, it is easy to show that when the flow possesses some symmetry in z, G must vanish.

For liquid metals used in laboratory experiments P_m is very small ($10^{-5} \sim 10^{-7}$). It is therefore reasonable to apply the inductionless limit approximation $P_m \to 0$ to the governing equations (see Davidson 2017, for example). The magnetic field perturbation is rescaled as $\widetilde{\mathbf{b}} = P_m^{-1/2} H^{-1} \widetilde{\mathbf{B}}$ and the size of the variables $\widetilde{\mathbf{v}}, \widetilde{\mathbf{b}}, \widetilde{p}$ and R_i, R_o, H are fixed as $O(P_m^0)$ quantities during the limiting process. The resulting leading-order equations are

$$\begin{bmatrix} (\partial_t + r^{-1} v_b \partial_\theta + R_p w_p \partial_z) \widetilde{u} - 2r^{-1} v_b \widetilde{v} \\ (\partial_t + r^{-1} v_b \partial_\theta + R_p w_p \partial_z) \widetilde{v} + r^{-1} (r v_b)' \widetilde{u} \\ (\partial_t + r^{-1} v_b \partial_\theta + R_p w_p \partial_z) \widetilde{w} \end{bmatrix}$$
$$- H^2 \begin{bmatrix} (r^{-1} B_b \partial_\theta + C_b \partial_z) \widetilde{a} - 2r^{-1} B_b \widetilde{b} \\ (r^{-1} B_b \partial_\theta + C_b \partial_z) \widetilde{b} + r^{-1} (r B_b)' \widetilde{a} \\ (r^{-1} B_b \partial_\theta + C_b \partial_z) \widetilde{c} \end{bmatrix} + (\widetilde{\mathbf{v}} \cdot \nabla) \widetilde{\mathbf{v}} = -\nabla \widetilde{p} + \nabla^2 \widetilde{\mathbf{v}}, \quad (2.7a)$$

$$- \begin{bmatrix} (r^{-1} B_b \partial_\theta + C_b \partial_z) \widetilde{u} \\ (r^{-1} B_b \partial_\theta + C_b \partial_z) \widetilde{v} - r(r^{-1} B_b)' \widetilde{u} \\ (r^{-1} B_b \partial_\theta + C_b \partial_z) \widetilde{w} \end{bmatrix} = \nabla^2 \widetilde{\mathbf{b}}, \qquad (2.7b)$$

along with the solenoidal conditions $\nabla \cdot \widetilde{\mathbf{v}} = \nabla \cdot \widetilde{\mathbf{b}} = 0$. The time derivative drops out from the induction equations on account of applying the inductionless limit, and (2.7b) becomes a mere linear system linking the velocity and the magnetic field. It can thus be used, as will be shown shortly, to eliminate the magnetic perturbation from the momentum equation (2.7a).

2.1. *Spectral discretisation on a parallelogram domain*

We shall be looking here for nonlinear travelling wave solutions of the above resulting equations. The hydrodynamic and magnetic perturbation fields $\widetilde{\mathbf{v}}$ and $\widetilde{\mathbf{b}}$ are both solenoidal, so they admit a *toroidal-poloidal* decomposition of the form

$$\widetilde{\mathbf{v}}(r, \theta, z, t) = \mathbf{e}_\theta \overline{v}(r) + \mathbf{e}_z \overline{w}(r) + \nabla \times \nabla \times \{\mathbf{e}_r \phi(r, \theta, z, t)\} + \nabla \times \{\mathbf{e}_r \psi(r, \theta, z, t)\}, (2.8a)$$

$$\widetilde{\mathbf{b}}(r, \theta, z, t) = \nabla \times \nabla \times \{\mathbf{e}_r f(r, \theta, z, t)\} + \nabla \times \{\mathbf{e}_r g(r, \theta, z, t)\}, \quad (2.8b)$$

where $\overline{v}(r)$ and $\overline{w}(r)$ are the azimuthal and axial components, respectively, of the mean velocity field. It can be easily shown that no mean magnetic field can be generated in the
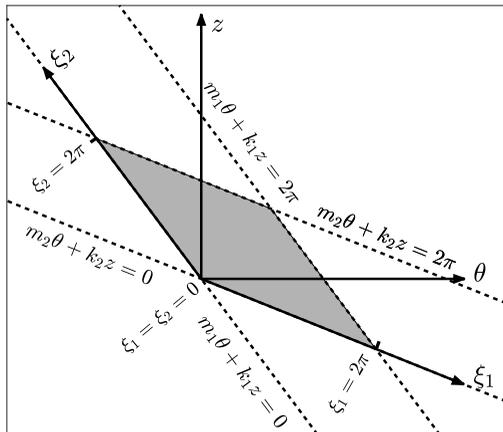
FIGURE 2. Sketch of the parallelogram domain introducing the new variables (ξ_1, ξ_2) that replace the usual azimuthal and axial coordinates (θ, z).

inductionless limit. The poloidal and toroidal potentials ϕ, f and ψ, g introduced in $(2.8a)$ and $(2.8b)$ uniquely determine the physical hydrodynamic and magnetic perturbation fields $\widetilde{\mathbf{v}}$ and $\widetilde{\mathbf{b}}$, except for the obvious gauge freedom (addition of a constant).

The coherent flows addressed in this work are mixed modes resulting from the nonlinear interaction of pairs of spiral waves propagating in the (θ, z)-plane. Following Deguchi & Altmeyer (2013), we introduce the two phase variables

$$\xi_1 = m_1\theta + k_1 z - c_1 t, \qquad \xi_2 = m_2\theta + k_2 z - c_2 t, \qquad (2.9)$$

describing the wavefronts of the two interacting spirals, which propagate at speeds c_1 and c_2, and whose azimuthal and axial wavenumbers are the integer (m_1, m_2) and real (k_1, k_2) constant pairs, respectively. Travelling mixed modes resulting from the nonlinear interaction of spiral modes of the form given by (2.9) are naturally represented on doubly 2π-periodic parallelogram domains of the form

$$(r, \xi_1, \xi_2) \in [r_i, r_o] \times [0, 2\pi] \times [0, 2\pi], \qquad (2.10)$$

unwrapped and outlined in figure 2 for any given value of the radial coordinate. Straightforward algebraic manipulation shows that any function of ξ_1, ξ_2 can also be written in terms of $\theta - c_\theta t$ and $z - c_z t$ with

$$c_\theta = \frac{k_2 c_1 - k_1 c_2}{m_2 k_1 - m_1 k_2}, \qquad c_z = \frac{m_2 c_1 - m_1 c_2}{m_2 k_1 - m_1 k_2}. \qquad (2.11)$$

The solutions sought are therefore travelling waves propagating both azimuthally and axially with the phase speeds c_θ and c_z just given, respectively.

The initial-boundary value problem $(2.7a)$-$(2.7b)$ is reformulated in the new phase variables assuming 2π-periodicity of the toroidal and poloidal potentials introduced in $(2.8a)$-$(2.8b)$

$$[\phi, \psi, f, g](r, \xi_1 + 2\pi, \xi_2) = [\phi, \psi, f, g](r, \xi_1, \xi_2 + 2\pi) = [\phi, \psi, f, g](r, \xi_1, \xi_2). \qquad (2.12)$$

The potentials are then discretised using spectral Fourier expansions of the form

$$\phi(r,\xi_1,\xi_2) = \sum_{n_1,n_2} \widehat{\phi}_{n_1 n_2}(r)\,\mathrm{e}^{\mathrm{i}(n_1\xi_1+n_2\xi_2)}, \quad \psi(r,\xi_1,\xi_2) = \sum_{n_1,n_2} \widehat{\psi}_{n_1 n_2}(r)\,\mathrm{e}^{\mathrm{i}(n_1\xi_1+n_2\xi_2)}, \quad (2.13a)$$

$$f(r,\xi_1,\xi_2) = \sum_{n_1,n_2} \widehat{f}_{n_1 n_2}(r)\,\mathrm{e}^{\mathrm{i}(n_1\xi_1+n_2\xi_2)}, \quad g(r,\xi_1,\xi_2) = \sum_{n_1,n_2} \widehat{g}_{n_1 n_2}(r)\,\mathrm{e}^{\mathrm{i}(n_1\xi_1+n_2\xi_2)}, \quad (2.13b)$$

where the Fourier radial functions $\widehat{\phi}_{n_1 n_2}(r)$, $\widehat{\psi}_{n_1 n_2}(r)$, $\widehat{f}_{n_1 n_2}(r)$, and $\widehat{g}_{n_1 n_2}(r)$ are identically zero for $n_1 = n_2 = 0$. For $n_1 \neq 0$ or $n_2 \neq 0$, these radial functions are suitable expansions of modified Chebyshev polynomials satisfying homogeneous no-slip boundary conditions at the inner and outer cylinder walls

$$\phi = \partial_r \phi = \psi = \overline{v} = \overline{w} = 0. \qquad (2.14)$$

The hydrodynamic radial functions are thus

$$\widehat{\phi}_{n_1 n_2}(r) = \sum_l X^{(1)}_{ln_1 n_2}(1-y^2)^2 T_l(y), \quad \widehat{\psi}_{n_1 n_2}(r) = \sum_l X^{(2)}_{ln_1 n_2}(1-y^2)T_l(y), \quad (2.15a)$$

$$\overline{v}(r) = \sum_l X^{(1)}_{l00}(1-y^2)T_l(y), \quad \overline{w}(r) = \sum_l X^{(2)}_{l00}(1-y^2)T_l(y), \quad (2.15b)$$

where $T_l(y)$ is the lth Chebyshev polynomial and $y \equiv 2(r-r_i)-1 \in [-1,1]$ is the rescaled radial coordinate. Similarly, the magnetic radial functions are expanded employing Chebyshev polynomials modified to satisfy perfectly insulating conditions

$$\widehat{f}_{n_1 n_2}(r) = \sum_l X^{(3)}_{ln_1 n_2}\left\{(1-y^2)T_l(y) + \alpha_{ln_1 n_2} + \beta_{ln_1 n_2}y\right\}, \qquad (2.16a)$$

$$\widehat{g}_{n_1 n_2}(r) = \gamma_{n_1 n_2}(r)\widehat{f}_{n_1 n_2}(r) + \sum_l X^{(4)}_{ln_1 n_2}(1-y^2)T_l(y), \qquad (2.16b)$$

where a detailed description of the coefficients $\alpha_{ln_1 n_2}$, $\beta_{ln_1 n_2}$, and of the function $\gamma_{n_1 n_2}(r)$ can be found in Appendix A.

For computational purposes, the Fourier-Chebyshev expansions (2.15a-2.16b) are truncated at $l = L$, $|n_1| = N_1$ and $|n_2| = N_2$. After substituting the truncated expansions into system (2.7a-2.7b), these are then evaluated at the Chebyshev nodes

$$y = \cos\left(\frac{l+1}{L+2}\pi\right), \qquad (l = 1,\ldots,L). \qquad (2.17)$$

This procedure leads to a system of nonlinear algebraic equations of the form

$$0 = \mathbb{L}_1 \begin{bmatrix} X^{(1)}_{ln_1 n_2} \\ X^{(2)}_{ln_1 n_2} \end{bmatrix} + H^2 \mathbb{L}_2 \begin{bmatrix} X^{(3)}_{ln_1 n_2} \\ X^{(4)}_{ln_1 n_2} \end{bmatrix} + [X^{(1)}_{ln_1 n_2}, X^{(2)}_{ln_1 n_2}]\mathbb{N} \begin{bmatrix} X^{(1)}_{ln_1 n_2} \\ X^{(2)}_{ln_1 n_2} \end{bmatrix}, \qquad (2.18a)$$

$$\mathbb{L}_3 \begin{bmatrix} X^{(1)}_{ln_1 n_2} \\ X^{(2)}_{ln_1 n_2} \end{bmatrix} = \mathbb{L}_4 \begin{bmatrix} X^{(3)}_{ln_1 n_2} \\ X^{(4)}_{ln_1 n_2} \end{bmatrix}. \qquad (2.18b)$$

Here $\mathbb{L}_1, \mathbb{L}_2, \mathbb{L}_3, \mathbb{L}_4$ are matrices, and $\mathbb{N}$ is a third-order tensor, whose form is unchanged from the purely hydrodynamic case. Isolating the magnetic unknowns by solving the linear system (2.18b) and substituting into (2.18a) yields a nonlinear system of equations for the hydrodynamic unknowns $X^{(1)}_{ln_1 n_2}$ and $X^{(2)}_{ln_1 n_2}$

$$0 = (\mathbb{L}_1 + H^2\mathbb{L}_2\mathbb{L}_4^{-1}\mathbb{L}_3)\begin{bmatrix} X^{(1)}_{ln_1 n_2} \\ X^{(2)}_{ln_1 n_2} \end{bmatrix} + [X^{(1)}_{ln_1 n_2}, X^{(2)}_{ln_1 n_2}]\mathbb{N}\begin{bmatrix} X^{(1)}_{ln_1 n_2} \\ X^{(2)}_{ln_1 n_2} \end{bmatrix}. \qquad (2.19)$$

Matrix $\mathbb{L}_1$ depends implicitly on the unknown speeds c_1 and c_2 appearing in (2.9) and that correspond to the co-moving reference frame in which the mixed mode remains a steady solution. Since these two speeds are also unknown, two additional *phase-locking* conditions are required to lift the rotational/travelling degeneracy of solutions from the system of equations. Similarly, system (2.19) must also be complemented with an additional constraint to allow determination of the unknown axial pressure-gradient G required to ensure the zero mass-flux condition. The nonlinear system of equations (2.19), along with the aforementioned constraints, is solved numerically using Newton's method. The hydrodynamic part of the code is identical to that used in Deguchi & Altmeyer (2013), and more detailed documentation of the computational methodology can be found in Deguchi & Nagata (2011).

For the purely hydrodynamic problem, we have also computed and continued in parameter space the bifurcating mixed modes using an independent numerical formulation. This alternative methodology is based on a solenoidal Petrov-Galerkin scheme described in Meseguer *et al.* (2007), suitably adapted to the annular parallelogram domain (2.10). In this formulation, the solenoidal velocity perturbation $\widetilde{\mathbf{v}}$ is approximated by means of a spectral expansion $\widetilde{\mathbf{v}}_s$ of order N in $\xi_1 = m_1\theta + k_1 z$, order L in $\xi_2 = m_2\theta + k_2 z$, and order M in r

$$\widetilde{\mathbf{v}}_s(r, \xi_1, \xi_2, t) = \sum_{n_1, n_2, m} a_{n_1 n_2 m}(t)\, \boldsymbol{\Phi}_{n_1 n_2 m}(r, \xi_1, \xi_2). \tag{2.20}$$

The $\boldsymbol{\Phi}_{n_1 n_2 m}$ are *trial* bases of solenoidal vector fields of the form

$$\boldsymbol{\Phi}_{n_1 n_2 m}(r, \xi_1, \xi_2) = \mathrm{e}^{\mathrm{i}(n_1 \xi_1 + n_2 \xi_2)} \mathbf{v}_{n_1 n_2 m}(r), \tag{2.21}$$

where the radial fields $\mathbf{v}_{n_1 n_2 m}(r)$ are suitably constructed to satisfy $\nabla \cdot \boldsymbol{\Phi}_{n_1 n_2 m} = 0$. Since $\widetilde{\mathbf{v}}_s$ represents the perturbation of the velocity field, it must therefore vanish at the inner ($r = r_i$) and outer ($r = r_o$) walls of the cylinders. Therefore, $\mathbf{v}_{n_1 n_2 m}$ must also satisfy homogeneous boundary conditions

$$\mathbf{v}_{n_1 n_2 m}(r_i) = \mathbf{v}_{n_1 n_2 m}(r_o) = \mathbf{0}. \tag{2.22}$$

These radial fields are built from suitable expansions of modified Chebyshev polynomials. After introducing expansion

$$\widetilde{\mathbf{v}}_s(r, \xi_1, \xi_2, t) = \sum_{n_1, n_2, m} a_{n_1 n_2 m}^{\mathrm{TW}} \mathrm{e}^{\mathrm{i} n_1 (\xi_1 - c_1 t)} \mathrm{e}^{\mathrm{i} n_2 (\xi_2 - c_2 t)} \mathbf{v}_{n_1 n_2 m}(r) \tag{2.23}$$

into the hydrodynamic equations, the weak formulation described in Meseguer *et al.* (2007) leads to a system of nonlinear algebraic equations for the unknown coefficients $a_{n_1 n_2 m}^{\mathrm{TW}}$, similar to (2.19), to which the zero mass-flux constraint is also imposed. The resulting system of equations were solved using a *matrix-free* Newton-Krylov method (Kelley 2003). The converged nonlinear solutions were then continued in parameter space using pseudo-arclength continuation schemes (Kuznetsov 2004). To avoid cluttering the paper with unnecessary detail and because of the intricacies that are inherent to the numerical approach undertaken, a detailed description of the method will be published separately.

In the classic rectangular domain, the Petrov-Galerkin solenoidal discretization has been successfully used in the numerical approximation of transitional flows in cylindrical geometries (Mellibovsky & Meseguer 2006) and in the computation of subcritical rotating waves in annular domains (Deguchi *et al.* 2014). In the latter study, the code was cross-checked against the codes used in the aforementioned Deguchi & Nagata (2011) and Deguchi & Altmeyer (2013). In §4, the favourable comparison of the nonlinear results

produced by the annular-parallelogram extension of the two independent codes based on completely different formulations serves as an unbeatable procedure for code validation. The results for the linear magnetic part of (2.19) has instead been checked against the linear results by Hollerbach *et al.* (2010) in the next section.

For a travelling wave solution, the absolute values of *torque* on the inner and outer cylinders are always equal and represent the angular momentum transport. The torque on the inner cylinder can be computed indistinctly as

$$T \equiv \{-r^3 \partial_r (r^{-1} \overline{v})\}|_{r=r_i} = -\{r^3 \partial_r (r^{-1} \overline{v})\}|_{r=r_o}, \tag{2.24}$$

while the torque on the outer cylinder is $-T$ to keep the inner and outer cylinder rotating at constant speeds. We have characterized all Newton-converged nonlinear solutions throughout by their torque normalised by the corresponding base-flow torque $T_b = \{-r^3 \partial_r (r^{-1} v_b)\}|_{r=r_i} = -\{r^3 \partial_r (r^{-1} v_b)\}|_{r=r_o}$

$$\tau = \frac{T}{T_b} = \frac{\partial_r (r^{-1} \overline{v})}{\partial_r (r^{-1} v_b)}\bigg|_{r=r_i, r_o}, \tag{2.25}$$

such that the normalized torque τ is unity for laminar cicular Couette flow.

3. The anti-cyclonic regime

Let us consider the normalised base magnetic fields

$$B_b(r) = \frac{r_i}{r}, \qquad C_b(r) = \delta \tag{3.1}$$

to reproduce both the axisymmetric HMRI and non-axisymmetric AMRI modes found in the anti-cyclonic regime by Hollerbach *et al.* (2010). The constant δ represents the strength of the axial magnetic field relative to the azimuthal field, which is induced by a current running through the inner cylinder, parallel to its axis.

Following Hollerbach *et al.* (2010), we fix the rotation ratio to $\widehat{\mu} = \Omega_o^*/\Omega_i^* = R_o \eta / R_i = 0.26$. Note that for the anti-cyclonic regime $\widehat{\mu}$ must remain in the interval $[0.25, 1]$, where the lower bound corresponds to the Rayleigh line $\widehat{\mu} = \eta^2 = 0.25$, while the upper bound embodies solid-body rotation. The quasi-Keplerian rotation regime frequently used in astrophysical studies on accretion disks is charcterized by $\widehat{\mu} = \eta^{3/2} \approx 0.35$. This rotation law results from applying Kepler's law to both the inner and outer cylinder angular velocities, which results in a fair approximation of a strictly Keplerian flow across the gap. The choice $\widehat{\mu} = 0.26$, used in the experimental demonstration of AMRI by Seilmayer *et al.* (2014) places the flow in the anti-cyclonic regime but very close to the boundary set by the Rayleigh line. Liu *et al.* (2006) used a locally periodic approach to show that there is a limiting value $\widehat{\mu} \approx 0.3$ above which HMRI halts, and the analysis was later extended by Kirillov *et al.* (2012) to AMRI. To what extent this limit is actually relevant to fully cylindrical flows is however still under debate (see Rüdiger & Hollerbach 2007; Child *et al.* 2015). The radius ratio of the cylinders is set to $\eta = 0.5$. For this particular value of η, our definitions of R_i and H become identical to the hydrodynamic Reynolds number and the Hartmann number, respectively, used by Hollerbach *et al.* (2010). Most importantly, the parameter range studied there is feasible in the PROMISE experiments, where both axisymmetric (Stefani *et al.* 2006, 2007; Rüdiger *et al.* 2006) and non-axisymmetric (Seilmayer *et al.* 2014) modes were actually realised. Travelling waves similar to those predicted in the numerical studies were indeed observed. These waves originate from absolute instability (even global), rather than mere convective, as shown by the comprehensive experimental study on HMRI by Stefani *et al.* (2009).

Having fixed $\widehat{\mu}$ and η, we have performed a linear stability analysis of the base flow by exploring the eigenspectrum of the linearized hydromagnetic equations for combinations of R_i, H, δ, and azimuthal-axial pairs (m, k) of the associated spiral eigenfunctions. We started by reproducing the neutral curves in the H–R_i plane for $\delta = 0, 0.02, 0.03, 0.04, 0.05$, and for the optimal axial wavenumber $k > 0$ that maximizes the growth rate. For $\delta = 0$, the instability originates from the symmetric spirals with opposite tilt ($m = \pm 1$). The primal effect of finite δ is the breaking of that reflection symmetry. Moreover, the axisymmetric mode ($m = 0$) emerges and for sufficiently large $\delta \approx 0.05$ it dominates over the non-axisymmetric modes. The non-axisymmetric modes are of AMRI origin, while the axisymmetric mode only becomes dominant for distinctly helical fields, which leaves a finite range of δ where all three modes compete. The neutral curves we have computed are in perfect agreement with figure 3 of Hollerbach *et al.* (2010), where it was already pointed out that, for $\delta \approx 0.04$, the critical Reynolds numbers of all three modes become comparable. Here we have identified that at $\delta = 0.0413$ there is a point where all three modes become neutral simultaneously, as clearly shown in figure 3.

For the sake of clarity, we shall focus on the computation and continuation of nonlinear solutions along the straight line across parameter space $R_i = (1896/128)H$ (green solid line in figure 3a) that passes through the triple critical point at $(H, R_i) = (128, 1896)$. Figure 3b depicts the bifurcation diagram corresponding to the 6 different nonlinear solution branches, as characterized by torque as a function of the Hartmann number. At the tricritical point, the three eigenmodes, $(m, k) = (0, 5.672)$, $(m, k) = (1, 4.672)$ and $(m, k) = (-1, 2.818)$, become neutral simultaneously. As anticipated by weakly nonlinear analysis, bifurcation of various mixed modes is therefore expected. The Newton method described in §2 does indeed converge to one or another of the nonlinear pure- or mixed-mode solutions when a suitably weighted superposition of the three neutral eigenmodes is taken as an initial guess. Solutions have initially been computed in this way in the close neighbourhood of the tricritical point and then continued as a function of H using either natural or pseudo-arclength continuation algorithms. Three of the solution branches, converged from single-mode initial guesses fed into the Newton method, correspond to helically-invariant travelling spiral waves (black curves in figure 3b). These solutions we have dubbed as SPI$_m$, with the subscript m (solid black line for $m = 0$, dashed for $m = 1$, dotted for $m = -1$) denoting the azimuthal wavenumber of the mode (see table 1). All three branches bifurcate supercritically from the base laminar flow. Since these solutions can be computed in the usual rectangular domain using regular coordinates (θ, z), we omit a detailed analysis.

Suitable proportions of the weights applied to the critical eigenmodes in generating the initial seeds for the Newton method have allowed computation of all three possible mixed-mode nonlinear solution branches (red curves in figure 3b). These mixed modes have been labeled as MIX$_{m_1}^{m_2}$, with the sub- and super- scripts representing the azimuthal wavenumber of the two interacting modes, and duly reported in table 1. As mentioned earlier, these mixed modes can only be identified using an appropriate annular-parallelogram domain, as the superposition of the two modes does not fit any rectangular domain of affordable size.

All three mixed-mode branches bifurcate supercritically. A very remarkable feature of these mixed modes is that some of them have larger torque than the spirals. This aspect is of special relevance to the study of astrophysical accretion disks, as it is a paramount requirement for the large outward angular momentum flux that is believed to be the key to the observed rate of inward mass accretion. The MIX$_{-1}^0$ mode possesses the largest torque of all mixed modes, as is also clear from the azimuthal mean flow distortion shown in figure 4 for $H = 140$, $(R_i, R_o) \approx (2074, 1078)$. Figure 5 shows the corresponding total
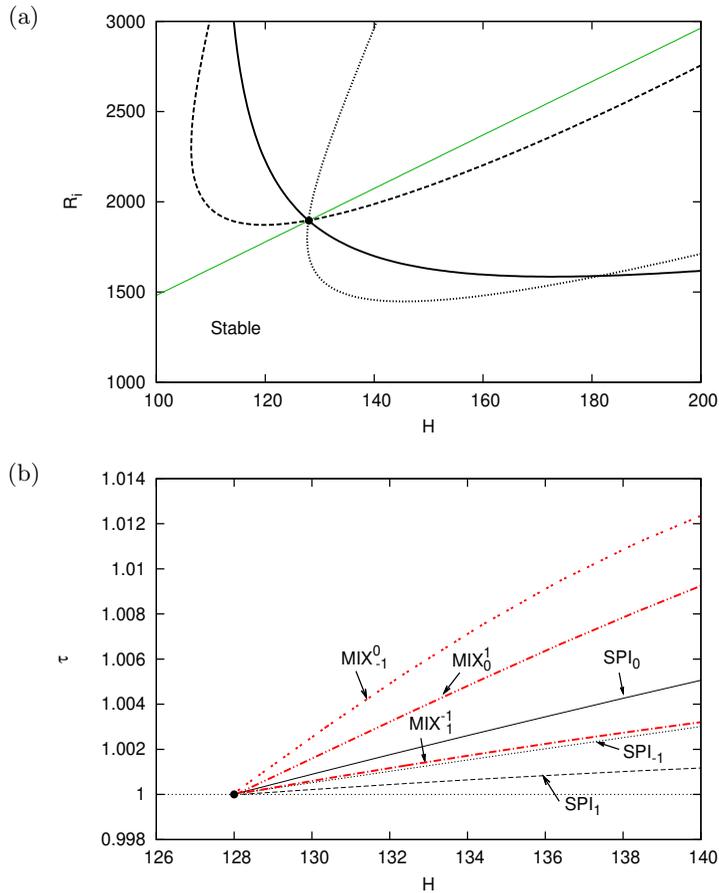
FIGURE 3. Linear stability analysis and continuation of bifurcated nonlinear solution branches in the anti-cyclonic regime for $(\delta, \eta) = (0.0413, 0.5)$. (a) Neutral stability curves along the line $R_o = 0.26 R_i / \eta$ (black curves) for modes $m = 0$ (solid) and $m = \pm 1$ (dashed for +1, dotted for -1). Wavenumber k is the one that maximises growth rate. The black circle indicates the triple critical point at $(H, R_i) = (128, 1896)$. (b) Bifurcation diagram along $R_i = (1896/128)H$ (green line in pannel a). The black circle corresponds again to the triple-critical point, whence three spiral (SPI$_0$, SPI$_{\pm 1}$; solid, dashed and dotted black lines) and three mixed (MIX$_1^{-1}$, MIX$_1^0$, MIX$_0^{-1}$; solid, dashed and dotted red lines) modes are issued.

azimuthal vorticity distribution of the three mixed modes, represented through θ–z plane colourmaps at mid gap $r = r_i + 0.5$. As expected, mode MIX$_{-1}^0$ has the strongest flow field perturbation, clearly reflected in the colour bar range of the panels. The visualisations shown in figures 5a and 5b for MIX$_0^1$ and MIX$_{-1}^0$, respectively, are reminiscent of wavy Taylor vortex flow (see e.g. Andereck *et al.* (1986)) except that the patterns are tilted and wavy vortex pairs accumulate an azimuthal phase shift as they pile up in the axial direction. The reason for this is that one of its constituents is a zero-pitch spiral, which corresponds to a toroidal-vortex-pair solution much like Taylor vortices, while the superposition of a spiral mode generates the tilted azimuthal modulation. Meanwhile, the structure of the MIX$_1^{-1}$ mode shown in figure 5c are evocative of the wavy spiral solution found in the hydrodynamic studies by Altmeyer & Hoffmann (2010) and Deguchi & Altmeyer (2013).

Figure No.	Abbreviation	Solution type	(m_1, k_1)	(m_2, k_2)
3b	SPI_0	Spiral	(0,5.672)	N/A
	SPI_1	Spiral	(1,4.672)	N/A
	SPI_{-1}	Spiral	(-1,2.818)	N/A
	MIX_0^{-1}	Mixed mode	(0,5.672)	(-1,2.818)
	MIX_1^{0}	Mixed mode	(1,4.672)	(0,5.672)
	MIX_1^{-1}	Mixed mode	(1,4.672)	(-1,2.818)
7a	SPI	Spiral	(1,40.6)	N/A
	SPI_{D17}	Spiral	(1,1.002)	N/A
	RIB	Ribbon	(1,40.6)	(-1,40.6)
	RIB_{D17}	Ribbon	(1,1.002)	(-1,1.002)
	MIX_+	Mixed mode	(1,40.6)	(1,1.002)
	MIX_-	Mixed mode	(1,40.6)	(-1,1.002)
7b	SPI_{D17}	Spiral	(1,0.616)	N/A
	SPI_{MRI}	Spiral	(1,1.984)	N/A
	RIB_{D17}	Ribbon	(1,0.616)	(-1,0.616)
	RIB_{MRI}	Ribbon	(1,1.984)	(-1,1.984)
	MIX_+	Mixed mode	(1,1.984)	(1,0.616)
	MIX_-	Mixed mode	(1,1.984)	(-1,0.616)

TABLE 1. Abbreviations used to describe the various nonlinear solution branches. Note that SPI_0 is a zero-pitch spiral, and therefore a toroidal-vortex-pair solution.
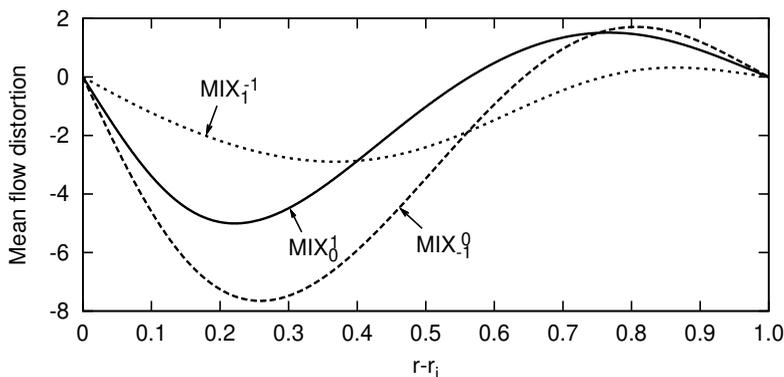

FIGURE 4. Azimuthal mean flow distortion $(\bar{v} - v_b)$ of the three different mixed modes shown in figure 3b for $H = 140$, and $(R_i, R_o) \approx (2074, 1078)$.

4. From counter-rotation to the cyclonic super-rotation regime

In this section we focus our attention on the bifurcations arising on the left-half plane of figure 1, as some of the instabilities carry on to the super-rotation regime. For $\eta = 0.1$, figure 6 outlines the neutral curves obtained from linear stability analyses corresponding to different levels of magnetization. We begin our analysis by first focusing on the purely hydrodynamic case in the absence of magnetic effects. Shown in figure 6 are the classical neutral curve (dashed black) alongside the neutral curve for the D17 mode (solid black), recently dicovered by Deguchi (2017) through linear stability analysis.
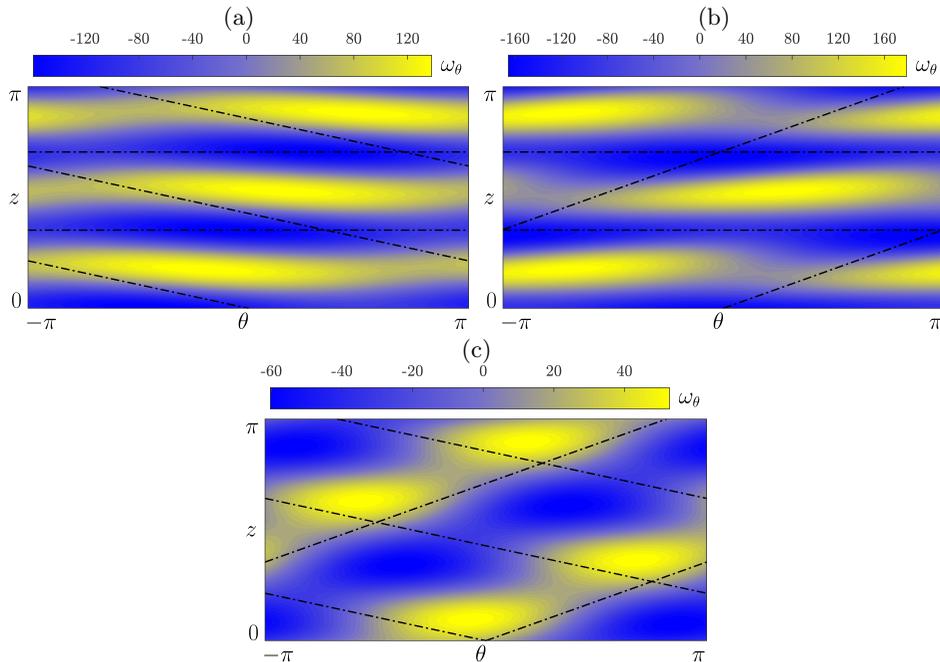
FIGURE 5. Colourmaps of the total azimuthal vorticity ($\omega_\theta = \partial_z u - \partial_r w$) distribution at the mid radial plane $r = r_i + 0.5$ of the three mixed-mode MRI solutions. (a) MIX^0_1, (b) MIX^0_{-1}, and (c) MIX^1_{-1}.

Along the classical boundary, the critical value of R_i increases with $|R_o|$, which is consistent with extensive numerical evidence as well as physical insights and the large Reynolds number formal asymptotic result (Esser & Grossmann 1996; Grossmann *et al.* 2016; Deguchi 2016). As a consequence, the neutral curve, which corresponds to a non-axisymmetric leading mode with large m (a spiral), cannot be continued across the line $R_i = 0$ into the super-rotation regime.

In contrast, the neutral curve for the D17 mode, typically with $m = \pm 1$, does indeed extend to the cyclonic super-rotation regime. The reason for choosing such a low value of the radius ratio ($\eta = 0.1$) follows from the observation that the curve shifts to very high counter-rotation rates as η is increased and narrower gaps are considered. For instance, taking $R_i = 0$ and $\eta = 5/7$ pushes the critical R_o value to $O(10^7)$, whereas for $\eta = 0.1$ it remains within order $O(10^4)$. In figure 6, the classical stability threshold (dashed black) and the new one set by the neutral curve of the D17 mode (solid black) meet at a bicritical point (black filled circle) located at $(R_i, R_o) \approx (1045, -10434)$, with associated critical wavenumbers $(m_1, k_1) = (1, 40.6)$ and $(m_2, k_2) = (1, 1.102)$, respectively. The critical axial wavenumbers k_1 and k_2 associated to either mode differ significantly, which explains why the latter, mode D17, escaped detection for so long. The asymptotic theory provided by Deguchi (2016) formally proved that the critical axial wavenumber of the classical mode gets asymptotically large for increasing Reynolds numbers, while that for the D17 mode seems to be insensitive to Reynolds number variations.

The various nonlinear solution branches that bifurcate from the bicritical point (black filled circle in figure 6) are shown in figure 7a. All branches bifurcate supercritically. The black curves correspond to the spiral solutions for the classical mode (SPI, dashed) and the D17 mode (SPI_{D17}, solid). The structure of the single-mode solutions, the nonlinear spirals, are qualitatively identical to the linear neutral mode (see Deguchi
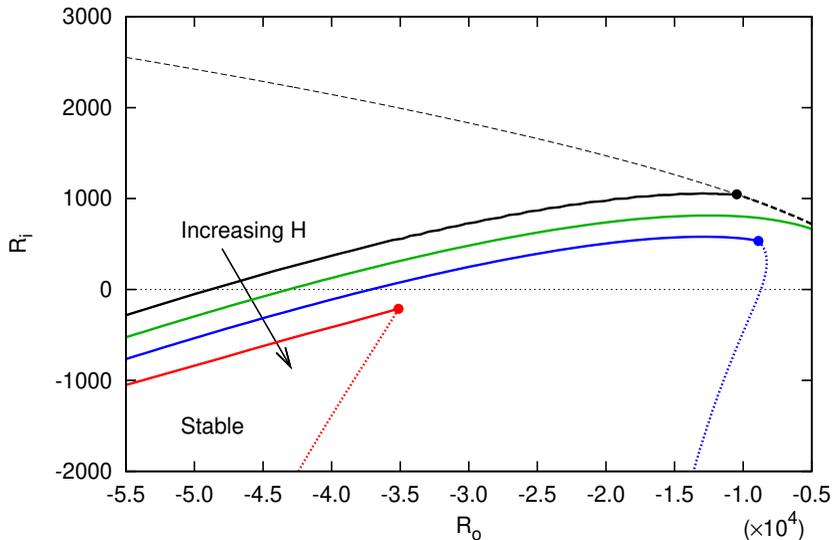
FIGURE 6. Neutral curves for $H = 0, 40, 60, 84$ (black, green, blue, red, respectively) and $\eta = 0.1$. The wavenumber pairs (k, m) are optimized to detect the most unstable eigenvalue. Neutral curve for the classical non-axisymmetric hydrodynamic mode (dashed black) is shown alongside those for the D17 mode (solid black) and the MRI mode (dotted). While m is large and obeys the asymptotic result by Deguchi (2016) for the classical neutral curve, the D17 and MRI neutral curves have typically $m = \pm 1$. Bicritical points, where direct bifurcation of mixed-mode solution branches are expected, are indicated with filled circles.

2017). Since the system is symmetric with respect to axial reflections $(z \to -z)$, spiral modes become neutral in pairs, with exact opposite pitch. As a result, there are actually four modes that simultaneously become neutral at the linear bicritical point (the black filled circle in figure 7a). Consequently, there exist six mixed modes arising from all possible combinations of modes taken in pairs. Two of them merely correspond to ribbon solutions (blue curves in figure 7a), labelled as RIB (dashed, SPI-SPI interaction) and RIB$_{D17}$ (solid, SPI$_{D17}$-SPI$_{D17}$ interaction), and listed in table 1. While ribbon solutions can be computed in a rectangular domain, all other mixed modes require the use of the annular-parallelogram domain. In fact, only two of the four remaining modes actually require computation, as the other two can be easily obtained from simple z-reflection and, since the torque is invariant under this symmetry operation, the solution branches are exactly coincident. The branches corresponding to these mixed-mode solutions are painted in red in figure 7a. The branch labelled as MIX$_+$ originates from the interaction of two modes with pitches of the same sign, while the one labelled MIX$_-$ arises from the nonlinear coupling of modes with opposite sign, as reported in table 1.

All hydrodynamic results reported in this work and initially computed with a code based on the hydromagnetic-potential formulation (2.13) have been reproduced using the independently developed solenoidal Petrov-Galerkin parallelogram formulation (2.20). A few nonlinear solutions at selected values of the parameters have been chosen and indicated with triangles in figure 7a to convey the excellent qualitative agreement between the two methods employed for the computations. Quantitative comparison shows that the torque discrepancy stays below 0.06% for all the purely hydrodynamic nonlinear mixed-mode solutions computed. Figure 8a represents the azimuthal mean flow distortion for the mixed modes at $(R_i, R_o) = (1100, -10434)$. The distortion is the most significant in
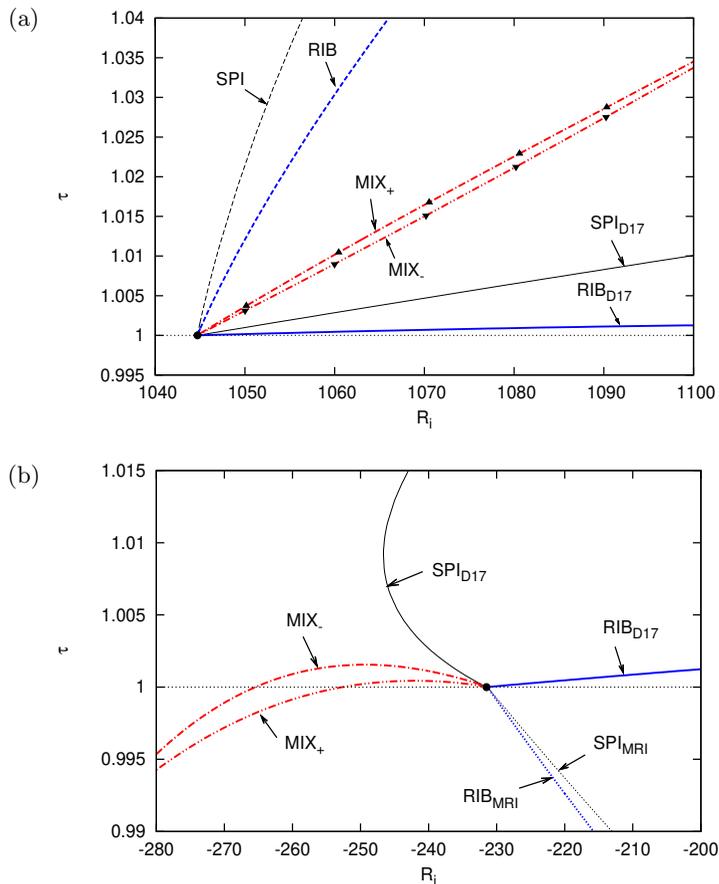
FIGURE 7. Bifurcation diagrams of spirals, ribbons and mixed nonlinear modes in super- and counter-rotation configurations. (a) Purely hydrodynamic case, in counter-rotation with $R_o = -10434$ and $H = 0$. The black circle indicates the linear bicritical point at $R_i = 1045$. A bunch of mixed-mode solutions computed with the alternative Petrov-Galerkin code are marked with triangles. (b) Magnetised case in the super-rotation regime with $R_o = -35150$ and $H = 84$. The bicritical point at $R_i = -231.5$ is indicated with a filled black circle.

the vicinity of the inner cylinder, which indicates that the perturbation is strongest in this region. For the same values of the parameters, figure 9 shows azimuthal vorticity colourmaps for both mixed modes on an unwrapped radial plane at $r = r_i + 0.05$. The observed flow structure is very different from any of the mixed-mode solutions reported by Deguchi & Altmeyer (2013). The observed small-large scale interaction reminds of the stripe pattern that is characteristic of intermittent spiral turbulence (Meseguer *et al.* 2009; Dong 2009). While the Reynolds numbers and the gap are too large to claim there exists any relation between the mixed modes presented here and spiral turbulence, the similarity of the patterns indicates that spiral turbulence might indeed be supported by mixed-mode solutions of very different pitches as the ones investigated here in a completely different setting.

   Now we turn our attention to the magnetised problem, where we will impose an external magnetic field with a strictly azimuthal orientation. For the MRI studies in an annulus, the azimuthal base magnetic field is typically the weighted superposition of r^{-1} and r components. The respective coefficients can be tuned by an appropriate uniform current
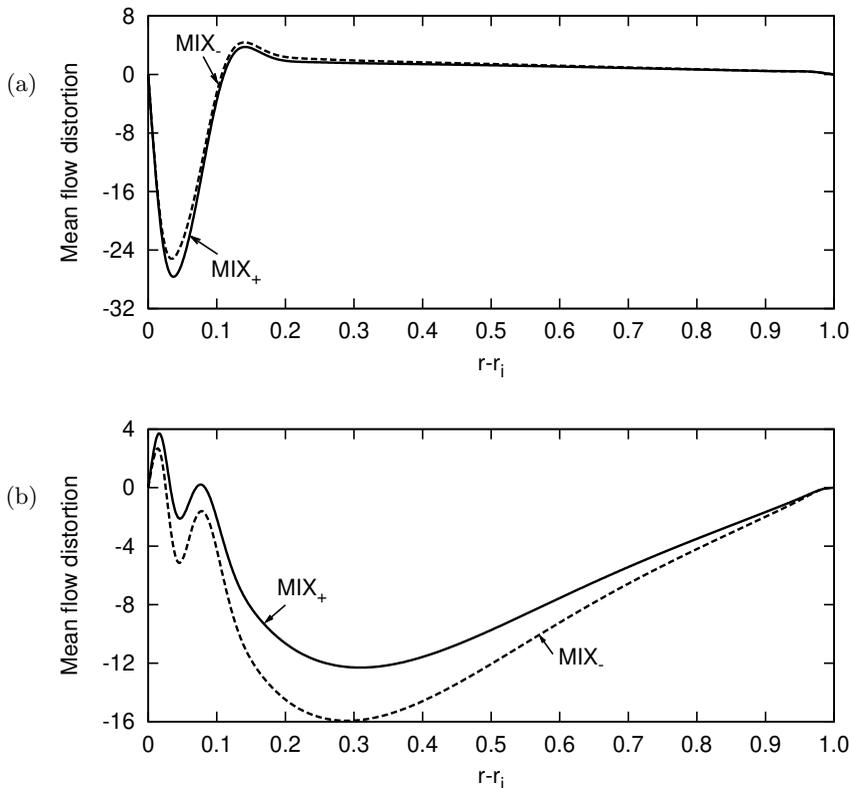
FIGURE 8. Azimuthal mean flow distortion $(\overline{v} - v_b)$ of mixed-mode solutions. (a) Purely hydrodynamic case at $R_i = 1100$ from figure 7a. (b) Magnetised case at $R_i = -280$ and $H = 84$ from figure 7b.

imposed within the inner and outer cylinders. Rüdiger *et al.* (2016, 2018*b*) considered two extreme cases: $B_b(r) \propto r^{-1}$ (i.e. there is no current between the cylinders) and $B_b(r) \propto r$ (i.e. the axial current is homogeneous between the cylinders). The latter also receives the alternative name *z*-pinch, and is known to become unstable for sufficiently large Hartmann number even with both cylinders at rest (Tayler 1957). As the *Tayler instability* does not exist for the current-free case, the behaviour of the neutral curve for small Reynolds numbers must necessarily be quite different from that for the homogeneous-current case. Rüdiger *et al.* (2016, 2018*b*) found that for $\eta \gtrsim 0.8$, the neutral curves behave qualitatively alike in both cases when Reynolds numbers are moderately large, thereby suggesting that super-AMRI is rather insensitive to the choice of the azimuthal magnetic field profile.

We have confirmed that the D17 mode is stabilised by both the current-free and the *z*-pinch cases. Nonetheless, when the two azimuthal magnetic field components exist simultaneously, the D17 mode can be destabilised, as clearly illustrated by the behaviour of the neutral stability curves in figure 6. Here the specific magnetic field profile used is

$$B_b(r) = \frac{r_i}{r} - \frac{r}{r_o}, \qquad C_b(r) = 0. \qquad (4.1)$$

Although the arguments by Rüdiger *et al.* (2016, 2018*b*) for the current-free case may not be applicable to the large gap $\eta = 0.1$ we tackle here, a MRI does indeed arise
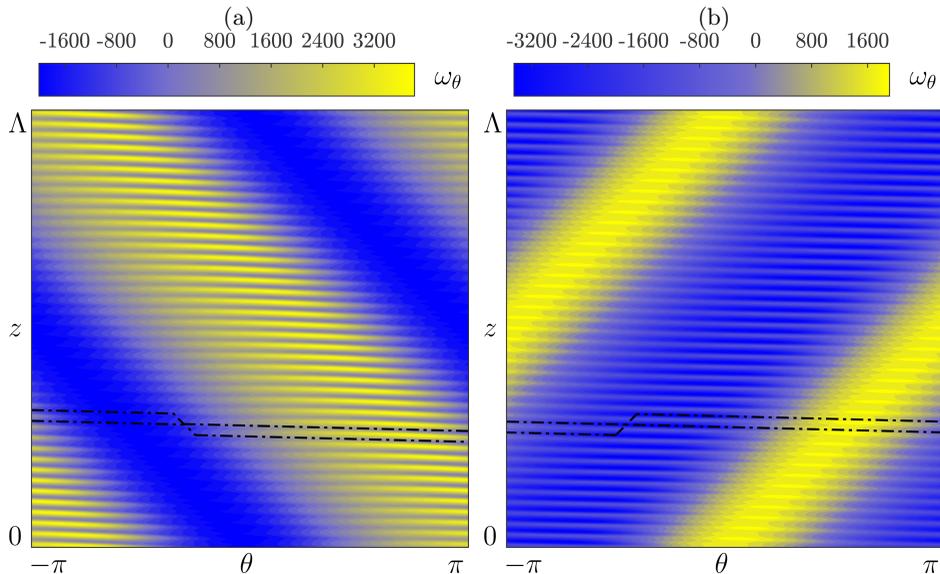
FIGURE 9. Visualisation of the total azimuthal vorticity ($\omega_\theta = \partial_z u - \partial_r w$) at $r = r_i + 0.05$ for the purely hydrodynamic mixed mode solutions at $R_i = 1100$ in Fig. 7(a). $\Lambda = 2\pi/1.002 \approx 6.27$. (a) MIX$_-$ and (b) MIX$_+$. The corresponding mean flow distortion was shown in Fig. 8(a).

when a current is considered. This phenomenon had already been anticipated by a locally periodic approach (see Liu *et al.* 2006; Kirillov *et al.* 2014), but the nature of the method used renders the approximation rather crude in view of the not-so-large critical wavenumbers we encounter here. As the Hartmann number is increased, the super-AMRI mode eventually takes over the classical mode, and hence changes the character of the bicritical point. In view of figure 6 at $H = 60$, the double critical point is already the result of the interaction of the D17 and the super-AMRI modes. The base flow remains stable within the region bounded by their respective stability thresholds. Along the combined neutral curve, the critical axial wavenumber experiences a discontinuous leap across the bicritical point, whence it must be inferred that the two instability mechanisms are indeed distinct. By further increasing the Hartmann number, the bicritical point moves towards and eventually crosses into the super-rotation regime. We have determined that the bicritical point crosses the $R_i = 0$ line somewhere between $H = 80$ and $H = 84$.

The nonlinear solution branches issued from the bicritical point $(R_i, R_o) \approx (-231.5, -35150)$ at $H = 84$ have been computed in the same way they were for the strictly hydrodynamic case studied above. The critical wavenumbers of the magnetised D17 mode at this point are $(m, k) = (1, 0.616)$, while those for the super-AMRI modes are $(m, k) = (1, 1.984)$, which entails flow structures of similar sizes. The bifurcation diagram of figure 7b has been obtained by varying R_i at constant R_o. To the right (left) of the linear critical point, the base flow is unstable to the D17 (super-AMRI) mode. The imposed azimuthal magnetic field does not break any of the inherent symmetries of the hydrodynamic Taylor-Couette system so that, as in the hydrodynamic case discussed above, there still arise two spirals (along with their mirror-images), two ribbons, and two mixed modes (and mirror images). See table 1 for an account of all modes. Both nonlinear spiral branches (black curves: solid for SPI$_{D17}$, dashed for SPI$_{MRI}$) bifurcate *subcritically*, in the sense that they exist when the corresponding linear mode is stable. However, this is only true while their amplitude remains small, and the branch associated with the D17 mode turns back in a saddle-node bifurcation towards lower $|R_i|$. The

RIB$_{\text{D17}}$ (solid blue) and RIB$_{\text{MRI}}$ (dashed blue) solution branches exist both to the right of the critical point (blue curves in figure 7b). We note in passing that the super-AMRI-type ribbon solutions found by Rüdiger *et al.* (2016) were shown stable by direct numerical simulation. The mixed-mode solution branches (red curves) come in two types, namely MIX$_+$ and MIX$_-$, depending on whether the interacting modes have the same or opposite pitch, respectively. Unlike all other solution branches issued from the bicritical point, these extend to large $|R_i|$, and may thus govern the dynamics within the region of the super-rotation regime closest to solid body rotation.

As clear from figure 7b, the nonlinear solution branches associated with the super-AMRI instability have the unforeseen property that the torque is reduced with respect to the laminar base value. The dependence of torque on Reynolds number associated with the two mixed modes follows very similar trends. The torque initially grows away from the bifurcation point as the branches dive deep into the super-rotation regime, but the trend is soon reversed and the torque eventually drops below laminar values.

The reason for torque reduction can be understood from the energy balance, since torque corresponds to one of the energy input mechanisms. The perturbation energy budget can be found by integrating $\widetilde{\mathbf{v}}\cdot(2.7a)+H^2\widetilde{\mathbf{b}}\cdot(2.7b)$. For travelling-wave-type solutions perturbation energy must be time-independent and thus the balance

$$\left\langle r\left(\frac{v_b}{r}\right)'\widetilde{u}\widetilde{v}\right\rangle - H^2\left\langle r^{-1}(rB_b)'(\widetilde{a}\widetilde{v}-\widetilde{u}\widetilde{b})\right\rangle = \langle\widetilde{\mathbf{v}}\cdot\nabla^2\widetilde{\mathbf{v}}\rangle + H^2\langle\widetilde{\mathbf{b}}\cdot\nabla^2\widetilde{\mathbf{b}}\rangle \qquad (4.2)$$

should be satisfied. Here the angle brackets denote integration over the annular-parallelogram domain. The first term in the right and left hand sides are related to the torque, since integration of $v_b\mathbf{e}_\theta\cdot(2.7a)$ yields

$$-\left\langle r\left(\frac{v_b}{r}\right)'\widetilde{u}\widetilde{v}\right\rangle = \langle v_b\mathbf{e}_\theta\cdot\nabla^2\widetilde{\mathbf{v}}\rangle \qquad (4.3)$$

and integration by parts of the first term in the right hand side results in

$$\langle\mathbf{v}\cdot\nabla^2\mathbf{v}\rangle = \left(r_o^{-1}R_o - r_i^{-1}R_i\right)T - \langle|\nabla\mathbf{v}|^2\rangle. \qquad (4.4)$$

The energy balance equation (4.2) then becomes

$$-H^2\langle\widetilde{\mathbf{b}}\cdot\nabla^2\widetilde{\mathbf{b}}\rangle - H^2\left\langle r^{-1}(rB_b)'(\widetilde{a}\widetilde{v}-\widetilde{u}\widetilde{b})\right\rangle = \left(r_o^{-1}R_o - r_i^{-1}R_i\right)T - \langle|\nabla\mathbf{v}|^2\rangle. \quad (4.5)$$

Showing that torque cannot decrease below the laminar value for purely hydrodynamic Taylor-Couette flow is a straightforward exercise, because the terms on the left hand side are identically zero. The calculus of variations can then be used to prove that the minimum value of the functional $\mathbf{F}(\mathbf{v}) = \langle|\nabla\mathbf{v}|^2\rangle$ under the divergence-free constraint for $\mathbf{v}$ is realised by the solution to the Stokes equation (see Doering & Gibbon 1995, for example), namely the laminar Couette solution. Imposing $\langle|\nabla\mathbf{v}|^2\rangle \geqslant \langle|\nabla\mathbf{v}_b|^2\rangle = \left(r_o^{-1}R_o - r_i^{-1}R_i\right)T_b$ on (4.4) demands that $\tau \geqslant 1$ for the purely hydrodynamic case.

Moreover, the balance equation further leads to the conclusion that torque reduction cannot occur at all if the base magnetic field is current free, as this entails that the second term in the left hand side of (4.5) is absent. The proof is again straightforward as integration by parts shows that $-H^2\langle\widetilde{\mathbf{b}}\cdot\nabla^2\widetilde{\mathbf{b}}\rangle$ is positive definite. The resulting inequality

$$\begin{aligned}\left(r_o^{-1}R_o - r_i^{-1}R_i\right)T &\geqslant \left(r_o^{-1}R_o - r_i^{-1}R_i\right)T + H^2\langle\widetilde{\mathbf{b}}\cdot\nabla^2\widetilde{\mathbf{b}}\rangle = \langle|\nabla\mathbf{v}|^2\rangle \\ &\geqslant \left(r_o^{-1}R_o - r_i^{-1}R_i\right)T_b,\end{aligned} \qquad (4.6)$$

yields again $\tau \geqslant 1$. This outlines the necessity of a base current field if torque reduction is to be observed.
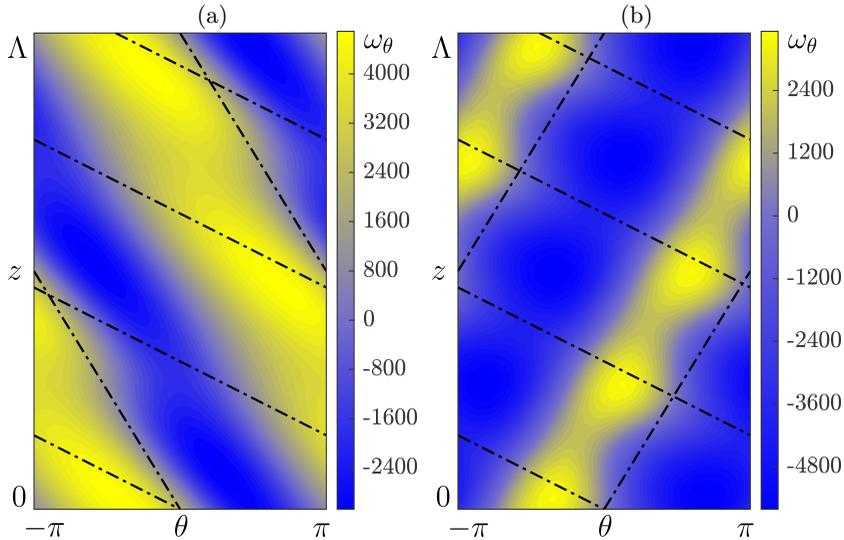
FIGURE 10. Visualisation of the total azimuthal vorticity ($\omega_\theta = \partial_z u - \partial_r w$) at $r = r_i + 0.05$ for the magnetized mixed mode solutions at $R_i = -280$ in Fig. 7(b). $\Lambda = 2\pi/0.616 \approx 10.2$ (a) MIX_ and (b) MIX+. The corresponding mean flow distortion was shown in Fig. 8(b).

As seen in figure 7b, the torque reduction is stronger for the MIX+ mode, reflecting the fact that the perturbation is slightly larger for that mode. This is evidenced by figure 8b, where the azimuthal mean flow distortion across the gap is plotted at $R_i = -280$. The oscillatory modulation of the flow near the inner cylinder is responsible for the torque reduction and is driven by the vortex structure near the inner cylinder, as shown in the θ-z sections of figure 10. Here again we choose $r = r_i + 0.05$, very close to the inner cylinder, as the reference radius. As expected, the perturbation of the MIX+ mode has larger amplitude than that for the MIX_ mode. The flow patterns are similar to those of the wavy spiral computed by Altmeyer & Hoffmann (2010) and Deguchi & Altmeyer (2013), because the critical wavenumbers of the interacting modes are of comparable size.

5. Conclusions

We have investigated nonlinear mode competitions in the MHD Taylor-Couette flow subject to predominantly azimuthal magnetic fields. For this purpose, a Newton solver devised by Deguchi & Altmeyer (2013) for the Navier-Stokes equations in annular-parallelogram domains has been extended for its application to the inductionless limit of the MHD equations.

For the anti-cyclonic regime (see figure 1), a suitably adjusted weak axial magnetic field in addition to the azimuthal field stimulates linear instability modes with $m = -1, 0, 1$, as anticipated by Hollerbach *et al.* (2010). Consistent with their results, we find particularly rich nonlinear dynamics for $\delta \simeq 0.04$. In section §3, we identified that there is a triple critical point involving all three modes for $\delta \approx 0.0413$. We have tracked the three nonlinear mixed-mode solution branches that bifurcate simultaneously at the triple critical point using the purposely devised Newton solver and arclength continuation. Some of the mixed-mode solutions possess a larger angular momentum transport (they require application of higher driving torque to keep the cylinders rotating) than the single-mode solutions they result from. This increased transport of angular momentum makes these mixed-mode solutions an interesting target for future study, as

they might be relevant in astrophysical flows involving accretion disks. In particular, a better understanding of what might their role be in the nonlinear dynamics of such flows will require direct numerical simulations and experiments such as those by PROMISE (Stefani *et al.* 2006, 2007; Rüdiger *et al.* 2006).

In §4, we have studied mode competitions involving the D17 mode. In the purely hydrodynamic case, there is a point where both the classical spiral mode and the D17 mode become neutral simultaneously. This bicritical point lies within the counter-rotation regime (see figure 1). The corresponding mixed-mode solutions consist of an interesting stripe pattern where the small-scale classical spirals are modulated by the larger-scale structure of the D17 mode. All purely hydrodynamic results presented here are in excellent agreement with analogous computations done with an independently developed Petrov-Galerkin code devised by Meseguer *et al.* (2007) and presently extended to allow computation of mixed-mode travelling-rotating wave solutions in annular-parallelogram domains. This code is better suited for the study of large-scale pattern formation in Taylor-Couette flow and includes not only travelling-rotating-waves Netwon-Krylov matrix-free solver (thus being capable of handling a much larger amount of degrees of freedom), but also stability analysis, a solver for modulated travelling-rotating waves and pseudo-arclength continuation of solution branches adapted from Mellibovsky & Meseguer (2015), and also direct numerical simulation. Details of this second code and its adaptation to annular-parallelogram domains will be presented in our future work in the study of large-scale pattern formation in Taylor-Couette flow. The intricacies of the method reach beyond the scope of the present study.

The application of an external azimuthal magnetic field alters the picture obtained in the purely hydrodynamic case completely. The non-axisymmetric super-AMRI mode found by Rüdiger *et al.* (2016, 2018*a*,*b*) appears at moderate Hartmann numbers and eventually outweighs the classical mode for sufficiently strong magnetic fields. We clearly show that the mechanisms behind the magnetised D17 mode and the super-AMRI mode are distinct. Destabilisation of the D17 mode occurs for a given external magnetic field profile (4.1). As a result, an increase of the Hartmann number gradually shifts the bicritical point at which both modes are simultaneously destabilised towards the super-rotation regime. This fact renders this mode interaction interesting from an astrophysical point of view. Several nonlinear solution branches are issued from the bicritical point in both R_i directions at fixed R_o. While spirals and ribbons return towards the counter-rotation regime, the mixed-mode solution branches plunge deep into the super-rotation regime.

The solutions computed in §4 show how the complex interplay between the nonlinear shear-Coriolis and the magneto-rotational instabilities can sometimes lead to torques lower than that of the base flow. This surprising result is in sharp contrast with what is typically assumed in purely hydrodynamic shear-flow studies, where nonlinearity is known to invariably enhance angular momentum transport. This torque reduction occurs even for finite P_m and sub-rotation of the cylinders; see Appendix B. In view of this result the torque reduction might be a generic property of MHD flows in the presence of shear and Coriolis forces. A particularly interesting potential application of this phenomenon would be to design control strategies to reduce drag on the curved boundary layers by imposing suitable magnetic fields.

We have analysed the D17 / super-AMRI mode interaction for a large gap $\eta = 0.1$. Interesting as it would be, we have not attempted here to track these modes to smaller annulus gaps in the order $\eta \sim 0.8$ and test the robustness of the coalescence point of both instabilities. The extremely large Reynolds numbers at which the D17 mode bifurcates in the narrow annulus case renders the task overly demanding from a computational point of view, if not altogether unaffordable.

Imposing more intense helical magnetic fields might also be an appealing topic for future research. The two axisymmetric super-HMRI modes found recently by Mamatsashvili *et al.* (2019), in combination with some of the modes studied here, may also yield rich interaction patterns worth exploring. While their type 2 super-HMRI mode belongs to the class of MRI requiring induction together with SMRI, the type 1 super-HMRI mode is inductionless and might therefore coexist with the super-AMRI mode and interact nonlinearly. Both types of super-HMRI modes might of course interact with the D17 mode. For HMRI, the further consideration of current in the fluid brings about even richer instability phenomena as anticipated by a locally periodic approach (Liu *et al.* 2006; Kirillov & Stefani 2013; Kirillov *et al.* 2014). The interaction of short wavelength modes found using the locally periodic approach with longer wavelength modes such as D17 or super-AMRI modes would generate band-like patterns much as those in figure 9.

Declaration of Interests. The authors report no conflict of interest.

6. Acknowledgements

Appendix A. Basis function for the magnetic potentials

Following Roberts (1964), we first determine the magnetic field for the outer zones $r < r_i$ and $r > r_o$. Within the perfectly insulating walls, the magnetic field must have a potential φ because there is no current:

$$\widetilde{a} = \varphi_r, \qquad \widetilde{b} = r^{-1}\varphi_\theta, \qquad \widetilde{c} = \varphi_z. \qquad (A\,1)$$

Since the magnetic field is solenoidal, the outer potential must satisfy Laplace's equation. Using the expansion

$$\varphi = \sum_{n_1,n_2} \widehat{\varphi}_{n_1 n_2}(r)e^{i(n_1\xi_1 + n_2\xi_2)}, \qquad (A\,2)$$

it is easy to find that the solution $\widehat{\varphi}_{n_1 n_2}(r)$ can be written down using the modified Bessel functions of the first and second kind, $I_\nu(x), K_\nu(x)$, both of which satisfy $x^2 f'' + xf' - (x^2 + \nu^2)f = 0$. The requirement that the potential is analytic at $r = 0$ determines the solution for $r < r_i$ as

$$\widehat{\varphi}_{n_1 n_2} = \begin{cases} I_{|A_{n_1 n_2}|}(|B_{n_1 n_2}|r) & \text{if} \quad |B_{n_1 n_2}| \neq 0, \\ \\ r^{|A_{n_1 n_2}|} & \text{if} \quad |B_{n_1 n_2}| = 0, \end{cases} \qquad (A\,3a)$$

whilst if the amplitude of the potential decays for large r, the solution for $r > r_o$ is

$$\widehat{\varphi}_{n_1 n_2} = \begin{cases} K_{|A_{n_1 n_2}|}(|B_{n_1 n_2}|r) & \text{if} \quad |B_{n_1 n_2}| \neq 0, \\ \\ r^{-|A_{n_1 n_2}|} & \text{if} \quad |B_{n_1 n_2}| = 0. \end{cases} \qquad (A\,3b)$$

Here we have used the shorthand notation $A_{n_1 n_2} = n_1 m_1 + n_2 m_2$ and $B_{n_1 n_2} = n_1 k_1 + n_2 k_2$. Note that the mean part $\widehat{\varphi}_{00}$ must be zero, from the boundary conditions.

Across the cylinder walls, the magnetic field must be continuous. Thus from (A 1) and the outer potential solutions (A 3), the boundary conditions are found as

$$\widehat{b}_{n_1 n_2} = \frac{A_{n_1 n_2}}{r_i B_{n_1 n_2}} \widehat{c}_{n_1 n_2} \qquad \widehat{a}_{n_1 n_2} + \frac{\mathrm{i} Q_{n_1 n_2}^-}{B_{n_1 n_2}} \widehat{c}_{n_1 n_2} = 0, \qquad \text{at} \quad r = r_i, \qquad (A\,4a)$$

$$\widehat{b}_{n_1 n_2} = \frac{A_{n_1 n_2}}{r_o B_{n_1 n_2}} \widehat{c}_{n_1 n_2} \qquad \widehat{a}_{n_1 n_2} + \frac{\mathrm{i} Q_{n_1 n_2}^+}{B_{n_1 n_2}} \widehat{c}_{n_1 n_2} = 0, \qquad \text{at} \quad r = r_o. \qquad (A\,4b)$$

Here $Q_{n_1 n_2}^{\pm}$ denotes the value of $\partial_r \widehat{\varphi}_{n_1 n_2} / \widehat{\varphi}_{n_1 n_2}$ on the walls:

$$Q_{n_1 n_2}^- = \begin{cases} \dfrac{|A_{n_1 n_2}|}{r_i} + \dfrac{|B_{n_1 n_2}| I_{|A_{n_1 n_2}|+1}(|B_{n_1 n_2}| r_i)}{I_{|A_{n_1 n_2}|}(|B_{n_1 n_2}| r_i)}, & \text{if} \quad |B_{n_1 n_2}| \neq 0, \\[4mm] \dfrac{|A_{n_1 n_2}|}{r_i}, & \text{if} \quad |B_{n_1 n_2}| = 0, \end{cases} \qquad (A\,5a)$$

$$Q_{n_1 n_2}^+ = \begin{cases} \dfrac{|A_{n_1 n_2}|}{r_o} - \dfrac{|B_{n_1 n_2}| K_{|A_{n_1 n_2}|+1}(|B_{n_1 n_2}| r_o)}{K_{|A_{n_1 n_2}|}(|B_{n_1 n_2}| r_o)}, & \text{if} \quad |B_{n_1 n_2}| \neq 0, \\[4mm] -\dfrac{|A_{n_1 n_2}|}{r_o}, & \text{if} \quad |B_{n_1 n_2}| = 0. \end{cases} \qquad (A\,5b)$$

After some algebra, we can find the boundary conditions for the poloidal and toroidal potentials as

$$\widehat{f}'_{n_1 n_2} + M_{n_1 n_2}^- \widehat{f}_{n_1 n_2} = 0, \qquad \widehat{g}_{n_1 n_2} - \gamma_{n_1 n_2}(r_i) \widehat{f}_{n_1 n_2} = 0 \qquad \text{at} \quad r = r_i \quad (A\,6a)$$

$$\widehat{f}'_{n_1 n_2} + M_{n_1 n_2}^+ \widehat{f}_{n_1 n_2} = 0, \qquad \widehat{g}_{n_1 n_2} - \gamma_{n_1 n_2}(r_o) \widehat{f}_{n_1 n_2} = 0 \qquad \text{at} \quad r = r_o, \quad (A\,6b)$$

where

$$\gamma_{n_1 n_2}(r) = \frac{2 A_{n_1 n_2} B_{n_1 n_2}}{B_{n_1 n_2}^2 r^2 + A_{n_1 n_2}^2}, \qquad (A\,7a)$$

$$M_{n_1 n_2}^- = \frac{r_i^2 B_{n_1 n_2}^2 - A_{n_1 n_2}^2}{r_i^2 B_{n_1 n_2}^2 + A_{n_1 n_2}^2} - \frac{r_i^2 B_{n_1 n_2}^2 + A_{n_1 n_2}^2}{r_i^2 Q_{n_1 n_2}^-}, \qquad (A\,7b)$$

$$M_{n_1 n_2}^+ = \frac{r_o^2 B_{n_1 n_2}^2 - A_{n_1 n_2}^2}{r_o^2 B_{n_1 n_2}^2 + A_{n_1 n_2}^2} - \frac{r_o^2 B_{n_1 n_2}^2 + A_{n_1 n_2}^2}{r_o^2 Q_{n_1 n_2}^+}. \qquad (A\,7c)$$

The second boundary conditions in (A 6) suggest that the functions $\widehat{g}_{n_1 n_2} - \gamma_{n_1 n_2} \widehat{f}_{n_1 n_2}$ must vanish on the walls, and thus we can use $(1 - y^2) T_l(y)$ to expand them. The function $\widehat{f}_{n_1 n_2}$ satisfies Robin's conditions on the walls as seen in the first boundary conditions in (A 6). As shown in Deguchi (2019b), we can use the following modified basis functions

$$(1 - y^2) T_l(y) + \alpha_{l n_1 n_2} + \beta_{l n_1 n_2} y, \qquad (A\,8)$$

where

$$\alpha_{l n_1 n_2} = 2 \frac{(-1)^l (1 + M_{n_1 n_2}^+) + (1 - M_{n_1 n_2}^-)}{(1 - M_{n_1 n_2}^-) M_{n_1 n_2}^+ - (1 + M_{n_1 n_2}^+) M_{n_1 n_2}^-}, \qquad (A\,9a)$$

$$\beta_{l n_1 n_2} = -2 \frac{(-1)^l M_{n_1 n_2}^+ + M_{n_1 n_2}^-}{(1 - M_{n_1 n_2}^-) M_{n_1 n_2}^+ - (1 + M_{n_1 n_2}^+) M_{n_1 n_2}^-}. \qquad (A\,9b)$$
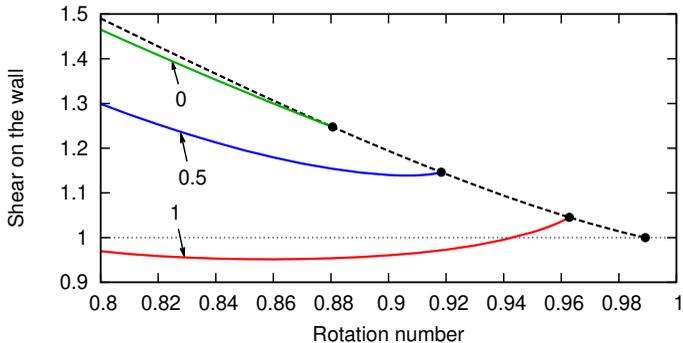
FIGURE 11. The narrow-gap computation for $P_m = 1$, $R = 400$, and the axial wavenumber $k = 3.117$. Dashed curve: Taylor vortex flow. Solid curves: the wavy vortex flow branches. The streamwise wavenumber (i.e. m/r_m at the narrow-gap limit) is 2.2. The values of B_0 are indicated by the arrows. Horizontal axis is the rotation number ω. In the vertical coordinate, the shear on the wall is normalized by its laminar value (i.e. τ at the narrow-gap limit).

Appendix B. Drag reduction of the wavy vortex flow

Here we show that the significant drag reduction observed in section 4 occurs even for the Rayleigh unstable sub-rotation regime (see figure 1). Moreover, the Prandtl number is not necessarily small to observe this phenomena; here we choose $P_m = 1$. The base magnetic field (4.1) is used.

We employ the narrow-gap limit $\eta \to 1$ in order to use the full MHD Cartesian code developed in Deguchi (2019a). Now we write $x = r_m\theta$, $y = (r - r_m)$ using the mid gap r_m. When η is close to unity, noting $y/r_m \ll 1$, we have approximations

$$v_b(r) - \Omega r = -Ry + \cdots, \qquad HB_b(r) = -B_0Ry + \cdots, \qquad (B1)$$

while keeping $\Omega = r_m^{-1}v_b(r_m)$, $R = 2r_m^{-2}R_p$ and $B_0 = H/R_p$ as $O((1-\eta)^0)$ constants. (Note that the definition of R differs by factor of 4 from that used in Deguchi (2019a), because in this paper the gap is 2.) The limiting system is the rotating plane Couette flow in the cartesian coordinate (x, y, z) with the rotation rate $\omega = 2\Omega/R$. The Rayleigh unstable region is $\omega \in [0, 1]$. For $B_0 \neq 0$, the flow is subjected to a linear magnetic field pointing in the streamwise direction.

The first few bifurcation sequence of hydrodynamic rotating plane Couette flow is widely acknowledged (see Nagata 1986; Daly et al. 2014, for example). Near the Rayleigh line $\omega = 1$, the Taylor-vortex flow bifurcates with the well-known axial critical wavenumber $k = 3.117$ as depicted by the dashed curve in Fig. 11. Further bifurcation of the green solid curve is due to the three-dimensional secondary instability of the Taylor-vortex and called the wavy-vortex flow.

The other solid curves in Fig. 11 (blue for $B_0 = 0.5$, red for $B_0 = 1$) show that with increasing B_0 the shear associated with the wavy vortex flow is eventually reduced even below the laminar value. Here note that this reduction only occurs when the flow is dependent on x (i.e. azimuthal direction). For example Taylor-vortex flow is x-independent, and thus the shear is unchanged whatever the value of B_0 is. This is because the cross-streamwise components of the magnetic field needed to modify the mean flow remains zero under the influence of the streamwise magnetic field.

REFERENCES

ALTMEYER, S. & HOFFMANN, C. 2010 Secondary bifurcation of mixed-cross-spirals connecting travelling wave solutions. *New J. Phys,* **12**, 113035–.

ANDERECK, C. D., LIU, S. S. & SWINNEY, H. L. 1986 Flow regimes in a circular Couette system with independently rotating cylinders. *J. Fluid Mech.* **164**, 155–.

AVILA, M., MESEGUER, A. & MARQUES, F. 2006 Double Hopf bifurcation in corotating spiral Poiseuille flow. *Phys. Fluids* **18**, 064101.

BALBUS, S. & HAWLEY, J. F. 1991 A powerful local shear instability in weakly magnetised disks. I. Linear analysis. *Astrophys. J.* **376**, 214–222.

BALBUS, S. A. 2017 When is high reynolds number shear flow not turbulent? *J. Fluid Mech.* **824**, 1–4.

BURIN, M. J. & CZARNOCKI, C. J. 2012 Subcritical transition and spiral turbulence in circular Couette flow. *JFM* **709**, 106–122.

CHANDRASEKHAR, S. 1960 The stability of non-dissipative Couette flow in hydromagnetics. *Proc. Nat. Acad. Sci.* **46**, 253–257.

CHILD, A., KERSALÉ, E. & HOLLERBACH, R. 2015 Nonaxisymmetric linear instability of cylindrical magnetohydrodynamic Taylor-Couette flow. *Phys. Rev. E* **92**, 033011.

CHOSSAT, P. & IOOSS, G. 1994 *The Couette-Taylor Problem*. Springer-Verlag.

COLES, D. 1965 Transition in circular Couette flow. *J. Fluid Mech.* **21**, 385–425.

DALY, C. A., SCHNEIDER, T. M., SCHLATTER, P. & PEAKE, N. 2014 Secondary instability and tertiary states in rotating plane Couette flow. *J. Fluid Mech.* **761**, 27–61.

DAVEY, A., DIPRIMA, R. C. & STUART, J. T. 1968 On the instability of Taylor vortices. *J. Fluid Mech.* **31**, 17–52.

DAVIDSON, P. A. 2017 *Introduction to Magnetohydrodynamics*, 2nd edn. Cambridge University Press.

DEGUCHI, K. 2016 The rapid-rotation limit of the neutral curve for Taylor-Couette flow. *J. Fluid Mech.* **808**, R2.

DEGUCHI, K. 2017 Linear instability in Rayleigh-stable Taylor-Couette flow. *Phys. Rev. E* **95**, 021102.

DEGUCHI, K. 2019*a* High-speed shear-driven dynamos. part 2. numerical analysis. *J. Fluid Mech.* **876**, 830–858.

DEGUCHI, K. 2019*b* High-speed standard magneto-rotational instability. *J. Fluid Mech.* **865**, 492–522.

DEGUCHI, K. & ALTMEYER, S. 2013 Fully nonlinear mode competitions of nearly bicritical spiral or Taylor vortices in Taylor-Couette flow. *Phys. Rev. E* **87**, 043017.

DEGUCHI, K., MESEGUER, A. & MELLIBOVSKY, F. 2014 Subcritical equilibria in Taylor-Couette flow. *Phys. Rev. Lett.* **112**, 184502.

DEGUCHI, K. & NAGATA, M. 2011 Bifurcations and instabilities in sliding Couette flow. *J. Fluid Mech.* **678**, 156–178.

DOERING, C. R. & GIBBON, J. D. 1995 *Applied Analysis of the Navier-Stokes Equations*. Cambridge University Press.

DONG, S. 2009 Evidence for internal structures of spiral turbulence. *Phys. Rev. E* **80**, 067301.

EDLUND, E. M. & JI, H. 2014 Nonlinear stability of laboratory quasi-keplerian flows. *Phys. Rev. E* **89**, 021004.

ESSER, A. & GROSSMANN, S. 1996 Analytic expression for Taylor-Couette stability boundary. *Phys. Fluids* **8**, 1814–1819.

GOLUBITSKY, M., STEWART, I. & SCHAEFFER, D. G. 1988 *Singularities and Groups in Bifurcation Theory*, *App. Math. Sci.*, vol. 2. New York: Springer.

GOODMAN, J. & JI, H. 2002 Magnetorotational instability of dissipative Couette flow. *J. Fluid Mech.* **462**, 365–382.

GROSSMANN, S., LOHSE, D. & SUN, C. 2016 High–Reynolds number Taylor-Couette turbulence. *Ann. Rev. Fluid Mech.* **48**, 53–80.

GUSEVA, A., WILLIS, A. P., HOLLERBACH, R. & AVILA, M. 2015 Transition to magnetorotational turbulence in Taylor–Couette flow with imposed azimuthal magnetic field. *New J. Phys.* **17**, 093018.

GUSEVA, A., WILLIS, A. P., HOLLERBACH, R. & AVILA, M. 2017 Transport properties of the azimuthal magnetorotational instability. *The Astrophysical Journal* **849**, 92.

HEGSETH, J. J., ANDERECK, C. D., HAYOT, F. & POMEAU, Y. 1989 Spiral turbulence and phase dynamics. *Phys. Rev. Lett.* **62(3)**, 257–260.

HERRON, I. & SOLIMAN, F. 2006 The stability of Couette flow in a toroidal magnetic field. *Appl. Math. Lett.* **19**, 1113–1117.

HOLLERBACH, R. & RÜDIGER, G. 2005 New type of magnetorotational instability in cylindrical Taylor-Couette flow. *Phys. Rev. Lett.* **95**, 124501.

HOLLERBACH, R., TEELUCK, V. & RÜDIGER, G. 2010 Nonaxisymmetric magnetorotational instabilities in cylindrical Taylor-Couette flow. *Phys. Rev. Lett.* **104**, 044502.

IOOSS, G. 1986 Secondary bifurcations of Taylor vortices into wavy inflow or outflow boundaries. *J. Fluid Mech.* **173**, 273–288.

JI, H., BURIN, M., SCHARTMAN, E. & GOODMAN, J. 2006 Hydrodynamic turbulence cannot transport angular momentum effectively in astrophysical disks. *Nature* **444**, 343–346.

KELLEY, C.T. 2003 *Solving nonlinear equations with Newton's method*. Philadelphia: SIAM.

KIRILLOV, O. N. & STEFANI, F. 2013 Extending the range of the inductionless magnetorotational instability. *Phys. Rev. Lett.* **111**, 061103.

KIRILLOV, O. N., STEFANI, F. & FUKUMOTO, Y. 2012 A unifying picture of helical and azimuthal magnetorotational instability, and the universal significance of the Liu limit. *The Astrophysical Journal* **756**, 83.

KIRILLOV, O. N., STEFANI, F. & FUKUMOTO, Y. 2014 Local instabilities in magnetized rotational flows: a short-wavelength approach. *J. Fluid Mech.* **760**, 591–633.

KUZNETSOV, Y. A. 2004 *Elements of Applied Bifurcation Theory, 3rd Ed.*. Springer-Verlag.

LIU, W., GOODMAN, J., HERRON, I. & JI, H. 2006 Helical magnetorotational instability in magnetized Taylor-Couette flow. *Phys. Rev. E* **74**, 056302.

LOPEZ, J. M. & AVILA, M. 2017 Boundary-layer turbulence in experiments on quasi-keplerian flows. *J. Fluid Mech.* **817**, 21–34.

MAMATSASHVILI, G., STEFANI, F., HOLLERBACH, R. & RÜDIGER, G. 2019 Two types of axisymmetric helical magnetorotational instability in rotating flows with positive shear. *Phys. Rev. Fluids* **4**, 103905.

MELLIBOVSKY, F. & MESEGUER, A. 2006 The role of streamwise perturbations in pipe flow transition. *Phys. Fluids* **18**, 074104.

MELLIBOVSKY, F. & MESEGUER, A. 2015 A mechanism for streamwise localisation of nonlinear waves in shear flows. *J. Fluid Mech.* **779**, R1.

MESEGUER, A., AVILA, M., MELLIBOVSKY, F. & MARQUES, F. 2007 Solenoidal spectral formulations for the computation of secondary flows in cylindrical and annular geometries. *Eur. Phys. J. Special Topics* **146**, 249–259.

MESEGUER, A., MELLIBOVSKY, F., AVILA, M. & MARQUES, F. 2009 Instability mechanisms and transition scenarios of spiral turbulence in Taylor-Couette flow. *Phys. Rev. E* **80**, 046315.

MICHAEL, D. 1954 The stability of an incompressible electrically conducting fluid rotating about an axis when current flows parallel to the axis. *Mathematika* **1**, 45–50.

NAGATA, M. 1986 Bifurcations in Couette flow between almost corotating cylinders. *J. Fluid Mech.* **169**, 229–250.

OSTILLA-MONICO, R., VERZICCO, R. & LOHSE, D. 2016 Turbulent Taylor-Couette flow with stationary inner cylinder. *J. Fluid Mech.* **799**, R1.

PINTER, A., LÜCKE, M. & HOFFMANN, C. 2006 Competition between traveling fluid waves of left and right spiral vortices and their different amplitude combinations. *Phys. Rev. Lett.* **96**, 044506.

PRIGENT, A., GREGOIRE, G., CHATE, H., DAUCHOT, O. & VAN SAARLOOS, W. 2002 Finite-wavelength modulation within turbulent shear flows. *Phys. Rev. Lett.* **89**, 014501.

RÜDIGER, G., GELLERT, M., HOLLERBACH, R., SCHULTZ, M. & STEFANI, F. 2018a Stability and instability of hydromagnetic Taylor–Couette flows. *Phys. Rep.* pp. 1–89.

RÜDIGER, G. & HOLLERBACH, R. 2007 Comment on "helical magnetorotational instability in magnetized Taylor-Couette flow". *Phys. Rev. E* **76**, 068301.

RÜDIGER, G., HOLLERBACH, R., STEFANI, F., GUNDRUM, T., GERBETH, G. & ROSNER, R. 2006 The traveling-wave MRI in cylindrical Taylor-Couette flow: comparing wavelengths and speeds in theory and experiment. *Astrophys. J.* **649**, L145–L147.

RÜDIGER, G., SCHULTZ, M., GELLERT, M. & STEFANI, F. 2016 Subcritical excitation of the current-driven Tayler instability by super-rotation. *Phys. Fluids* **28**, 014105.

RÜDIGER, G., SCHULTZ, M., GELLERT, M. & STEFANI, F. 2018*b* Azimuthal magnetorotational instability with super-rotation. *J. Plasma Phys.* **84**, 735840101.

SEILMAYER, M., GALINDO, V., GERBETH, G., GUNDRUM, T., STEFANI, F., GELLERT, M., RÜDIGER, G., SCHULTZ, M. & HOLLERBACH, R. 2014 Experimental evidence for nonaxisymmetric magnetorotational instability in a rotating liquid metal exposed to an azimuthal magnetic field. *Phys. Rev. Lett.* **113**, 024505.

STEFANI, F., GERBETH, G., GUNDRUM, T., HOLLERBACH, R., PRIEDE, J., RÜDIGER, G. & SZKLARSKI, J. 2009 Helical magnetorotational instability in a taylor-couette flow with strongly reduced ekman pumping. *Phys. Rev. E* **80**, 066303.

STEFANI, F., GUNDRUM, T., GERBETH, G., RÜDIGER, G., SCHULTZ, J., SZKLARSKI, J. & HOLLERBACH, R. 2006 Experimental evidence for magnetorotational instability in a Taylor-Couette flow under the influence of a helical magnetic field. *Phys. Rev. Lett.* **97**, 184502.

STEFANI, F., GUNDRUM, T., GERBETH, G., RÜDIGER, G., SZKLARSKI, J. & HOLLERBACH, R. 2007 Experiments on the magnetorotational instability in helical magnetic fields. *New J. Phys.* **9**, 295–.

STEFANI, F. & KIRILLOV, O. N. 2015 Destabilization of rotating flows with positive shear by azimuthal magnetic fields. *Phys. Rev. E* **92**, 051001.

TAGG, R., EDWARDS, W. S., SWINNEY, H. L. & MARCUS, P. S. 1989 Nonlinear standing waves in Couette-Taylor flow. *Phys. Rev. A* **39**, 3734–3737.

TAYLER, R. J. 1957 Hydromagnetic instabilities of an ideally conducting fluid. *Proc. Roy. Phys. Soc.* **70**, 31–48.

TAYLOR, G. I. 1923 Stability of a viscous fluid contained between two rotating cylinders. *Phil. Trans. R. Soc. A* **223**, 289–343.

VAN ATTA, C. 1966 Exploratory measurements in spiral turbulence. *J. Fluid Mech.* **25**, 495–.

VELIKHOV, E. P. 1959 Stability of an ideally conducting liquid flowing between cylinders rotating in a magnetic field. *Soviet. Phys. JETP* **36**, 1389–1404.

WENDT, F. 1933 Turbulente strömungen zwischen zwei rotierenden koaxialen zylindern. *Ing.-Arch.* **4**, 577–595.